Stratigraphy and geochronological constraints of the Serra Sul Formation (Carajás Basin, Amazonian Craton, Brazil)

Camille Rossignol, Eric Siciliano Rego, Francesco Narduzzi, Lívia Teixeira, Janaína N Ávila, Marco Silva, Cristiano Lana, Pascal Philippot

Journal Pre-proofs

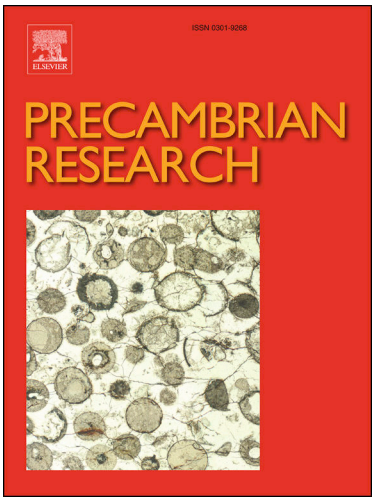

Stratigraphy and geochronological constraints of the Serra Sul Formation (Carajás Basin, Amazonian Craton, Brazil)

Camille Rossignol, Eric Siciliano Rego, Francesco Narduzzi, Lívia Teixeira, Janaína N. Ávila, Marco A.L. Silva, Cristiano Lana, Pascal Philippot

PII: S0301-9268(20)30570-2
DOI: https://doi.org/10.1016/j.precamres.2020.105981
Reference: PRECAM 105981

To appear in: *Precambrian Research*

Received Date: 1 May 2020
Revised Date: 14 September 2020
Accepted Date: 21 October 2020

Please cite this article as: C. Rossignol, E. Siciliano Rego, F. Narduzzi, L. Teixeira, J.N. Ávila, M.A.L. Silva, C. Lana, P. Philippot, Stratigraphy and geochronological constraints of the Serra Sul Formation (Carajás Basin, Amazonian Craton, Brazil), *Precambrian Research* (2020), doi: https://doi.org/10.1016/j.precamres.2020.105981

Stratigraphy and geochronological constraints of the Serra Sul Formation (Carajás Basin, Amazonian Craton, Brazil)

Camille Rossignol[a, b]*, Eric Siciliano Rego[b, c], Francesco Narduzzi[a, d], Lívia Teixeira[a], Janaína N. Ávila[e], Marco A. L. Silva[f], Cristiano Lana[f], Pascal Philippot[a, b, d]

[a]*Departamento de Geofísica, Instituto de Astronomia, Geofísica e Ciências Atmosféricas da Universidade de São Paulo - IAG-USP, Rua do Matão, 1226 - Cidade Universitária, Butantã, 05508-090 São Paulo – SP, Brazil*

[b]*Institut de Physique du Globe de Paris, Université de Paris, CNRS, Paris, France*

[c]*Instituto de Geociências, Universidade de São Paulo, Rua do Lago, 562 - Cidade Universitária, São Paulo, 05508-080, Brazil*

[d]*Géosciences Montpellier, Université de Montpellier, CNRS, Université des Antilles, Montpellier, France*

[e]*Research School of Earth Sciences, The Australian National University, 142 Mills Road, Canberra ACT 2601, Australia*

[f]*Applied Isotope Research Group, Departamento de Geologia, Escola de Minas, Universidade Federal de Ouro Preto, Rua Diogo de Vasconcelos, 122, 35400-000 Ouro Preto – MG, Brazil*

**Corresponding author: camil.rossignol@gmail.com*

ersiciliano@usp.br; france.nardo@iag.usp.br; liviateixeira@usp.br; janaina.avila@anu.edu.au; marcomineral@gmail.com; cristianodeclana@gmail.com; pascal.philippot@umontpellier.fr

Abstract

The Carajás Basin, Amazonian Craton, hosts extensive Neoarchean to Paleoproterozoic sedimentary archives, which are still poorly constrained regarding their depositional settings, ages, and type of basin in which they have been deposited. In this study, we performed detailed sedimentological investigations and U-Pb dating of detrital zircon in four drill cores intercepting the recently defined Serra Sul Formation. Our data show that this formation corresponds to various shallow to deep subaqueous environments. Shallow water environments are characterized by local occurrences of microbially-mediated structures, while deep water environments are characterized by polymictic conglomerates resulting from the mixing of materials of different origins during downslope debris flow. Both sedimentary facies and common occurrence of syn-sedimentary deformations attest for recurrent slope instabilities. Geochronological investigations allow to define a maximum depositional age of 2684 $\pm$ 10 Ma, that is several tens million years younger than other Neoarchean sedimentary units of the Carajás Basin. Major peaks in age distribution indicate that the Serra Sul Formation derives from local sources that constitute the basement of the Carajás Basin. The infilling of the Carajás Basin by local sources, together with sedimentary facies and depositional environments attesting for slope instabilities, suggest that the Serra Sul Formation was deposited during an active extensional tectonic phase. Such Neoarchean to early Paleoproterozoic tectonic setting compares with those documented in many other cratons worldwide and suggests that it could correspond to the break-up of one of the first documented supercontinent.

Keywords

Paleoenvironmental reconstruction; U-Pb geochronology; Detrital zircon; Diamictite, Supervaalbara.

1. Introduction

The Neoarchean to Paleoproterozoic (ca. 2.7 to ca. 2.1 Ga) represents a pivotal period for the Earth system (Eriksson et al., 2005; Reddy and Evans, 2009). During this period, global geodynamic evolved towards a modern-style plate tectonic (Chowdhury et al., 2017; Condie and Kröner, 2013; Dhuime et al., 2015). Growing lines of evidence support that major cratons were contiguous during the Neoarchean to early Paleoproterozoic, potentially forming a supercontinent that progressively broke up into several continents that drifted apart during the course of the Paleoproterozoic (Gumsley et al., 2017; Pesonen et al., 2003; Salminen et al., 2019). The secular cooling of the Earth induced a change of continental lithosphere rheology during the Neoarchean that allowed for the development of significant subaerial landmasses (Bindeman et al., 2018; Flament et al., 2008). The emergence of continents has been suggested to be linked, through biosphere mediation, to the rise of O_2 in the atmosphere and the oceans, which ultimately ended up with the Great Oxygenation Event between 2.5 Ga and 2.2 Ga (Campbell and Allen, 2008; Kump and Barley, 2007; Lyons et al., 2014; Philippot et al., 2018). The emergence of subaerial landmasses also allowed for continental weathering and subsequent drawdown of atmospheric CO_2 (Claire et al., 2006; Gumsley et al., 2017; Teitler et al., 2014). The increase of O_2 combined to the drawdown of CO_2 in the atmosphere triggered the appearance of glacial conditions, marked by three to four discrete glacial events

over a few hundred of million years (from ca. 2.45 Ga to ca. 2.22 Ga; e.g., Caquineau et al., 2018; Rasmussen et al., 2013).

Despite recent advances documenting the tectonic evolution of the Amazonian Craton (Fig. 1A; Tavares et al., 2018) and the stratigraphy of the Carajás Basin, located to the east of the craton (Fig. 1B; Araújo Filho et al., 2020; Araujo and Nogueira, 2019), the overall Neoarchean to early Paleoproterozoic geodynamic context of the eastern Amazonian Craton remains poorly constrained. For instance, glaciogenic sediments have recently been reported in the Serra Sul Formation (Fig. 2; Araujo and Nogueira, 2019), but little stratigraphic description have been provided for this formation. No age constraint is available for the Serra Sul Formation, while such data are critical for correlations with other sedimentary units across the world. In addition, the type of basin in which the Serra Sul Formation was deposited has not been investigated.

In this study, we performed detailed stratigraphic and geochronological analyses in the Serra Sul Formation. Sedimentological investigations indicate that this formation has been deposited under various subaqueous environments ranging from shallow to deep water settings characterized by slope instability and gravity flow processes. Geochronological analyses, performed on a large number of detrital zircon grains (1222 analyses), allows to define a maximum depositional age for the Serra Sul Formation of 2684 ± 10 Ma. Major peaks in age distribution indicate that the Serra Sul Formation derives from local sources forming the basement of the Carajás Basin. The infilling of the Carajás Basin by local sources, the sedimentary facies, as well as the depositional environments of the Serra Sul Formation, suggest that it has been deposited during an active extensional tectonic phase.

2. Geological setting

2.1. Regional context

The Carajás Domain corresponds to an elongated, E-W oriented, structural domain (Fig. 3; Tavares et al., 2018; Vasquez and Rosa-Costa, 2008). It hosts major ore deposits, including iron oxide-gold-copper deposits (e.g., Grainger et al., 2008; Marschik et al., 2005; Melo et al., 2014; Moreto et al., 2015; Pollard et al., 2019; Requia et al., 2003; Tassinari et al., 2003), Banded Iron Formations (BIFs; Dalstra and Guedes, 2004; Klein and Ladeira, 2002) and Mn ore deposits (Peters et al., 1977). The basement of the Carajás Domain consists of mafic granulites, migmatites and metavolcanic rocks with a protolith age of ca. 3.08-3.00 Ga and metamorphic ages of ca. 2.86 Ga (Machado et al., 1991; Moreto et al., 2015; Pidgeon et al., 2000). This basement was latter intruded by tonalites, trondhjemites and granodiorites (TTG) between ca. 2960 Ma and ca. 2930 Ma (Feio et al., 2013). Various magmatic rocks also intruded the basement at ca. 2.76 to 2.63 Ga (Feio et al., 2013, 2012; Machado et al., 1991; Melo et al., 2017; Sardinha et al., 2006), and a volcaniclastic succession was deposited at 2774 ± 19 Ma to the north of the Carajás Domain (Toledo et al., 2019). Two minor magmatic events later affected the Carajás Domain, at 2701 ± 30 Ma (Melo et al., 2017) and at ca. 2.5 Ga (Toledo et al., 2019). This 2.5 Ga magmatic event was associated with a long lasting tectono-thermal event that occurred between ca. 2600 and 2450 Ma (Grainger et al., 2008; Machado et al., 1991; Melo et al., 2017; Requia et al., 2003; Tallarico et al., 2005; Toledo et al., 2019). This episode remains poorly characterized and it is mainly documented by metamorphic ages (Grainger et al., 2008; Machado et al., 1991; Requia et al., 2003; Tallarico et al., 2005).

To the south, the Carajás Domain is delimited by the Canaã dos Carajás Shear Zone, which marks the boundary with the Rio Maria Domain (Fig. 3A). The latter comprises Mesoarchean rocks, including greenstone belts with komatiites (Siepierski and Ferreira Filho, 2016) and TTG emplaced between ca. 2.98 Ga and ca. 2.92 Ga (Almeida et al., 2013) and sanukitoid suites emplaced between ca. 2.87 Ga and ca. 2.86 Ga (Almeida et al., 2013; Althoff et al., 2014; Feio et al., 2013; Macambira and Lancelot, 1996). The welding between the Rio Maria and the Carajás domains occurred during the end of the Mesoarchean, between ca. 2.87 Ga and ca. 2.83 Ga (Tavares et al., 2018).

To the north, the Carajás Domain is separated from the Bacajá Domain (Fig. 3A) by the Cinzento Strike-Slip System, which had a protracted activity with several phases of dextral and sinistral movements (Pinheiro and Holdsworth, 1997). The basement of the Bacajá Domain is made up of ca. 2670 Ma tonalites and greenstone belts with metavolcanics rocks emplaced between ca. 2360 and ca. 2340 Ma (Macambira et al., 2009). The Bacajá Domain was later intruded by a series of Rhyacian granitoids from ca. 2220 Ma to ca. 2080 Ma (Macambira et al., 2009). The collision between the Bacajá and the Carajás domains took place during the Rhyacian, at ca. 2.1 Ga (Macambira et al., 2009; Tavares et al., 2018).

To the west, the Carajás Domain is overlain by volcanic and volcaniclastic rocks of the Uatumã Supergroup (Fig. 3A; Roverato, 2016; Roverato et al., 2017). These units belong to the Uatumã Silicic Large Igneous Province (SLIP; Antonio et al., 2017), which also includes A-type granitoids intrusive into the basement of the Carajás and Rio Maria domains (Teixeira et al., 2019). Age constraints obtained on volcanic and plutonic rocks and dykes indicate that the Uatumã SLIP was emplaced during a short period of time, between ca. 1.89 and 1.86 Ga (Antonio et al., 2017; Dall'Agnol et al., 2005; Machado et al., 1991; Roverato, 2016; Silva et al., 2016; Teixeira et al., 2019).

To the east, the Carajás Domains is bounded by the N-S Araguaia Belt (Fig. 3A), which formed the eastern margin of the Amazonian Craton during the Neoproterozoic (Hodel et al., 2019). This margin was inverted during the end of the Neoproterozoic (de Almeida et al., 2000) in response to the collision between the Amazonian Carton, the West African Craton, the Paranaíba Block, and the São Francisco Craton (Fig. 1A).

During the Neoarchean and Paleoproterozoic, different tectonic events affected the basement and overlying supracrustal units of the Carajás Province, resulting in a WNW trending strike-slip system (Pinheiro and Holdsworth, 1997). These major faults and shear zones were sealed by the intrusion of the 1.88 Ga old granitoids of the Uatumã SLIP (Pinheiro and Holdsworth, 1997). With the exception of two magmatic events at ca. 535 Ma and ca. 200 Ma post-dating the collision along the Araguaia Belt and the Central Atlantic Magmatic Province, respectively (Teixeira et al., 2019), the Carajás Domain remained relatively stable since 1.88 Ga.

2.2. Stratigraphic framework

Different stratigraphic subdivisions have been proposed (e.g., Araujo and Nogueira, 2019; Klein and Ladeira, 2002; Machado et al., 1991; Tavares et al., 2018; Trendall et al., 1998). Because the Carajás Basin has been discovered relatively recently (Tolbert et al., 1971) and is localized in a rather remote and poorly exposed region covered by dense vegetation and thick weathering profiles, stratigraphic studies have been notoriously difficult to achieve. The lack of accurate stratigraphic framework for the Carajás Basin has caused several units to be neglected or misinterpreted and new stratigraphic subdivisions are regularly proposed to account for new discoveries and better understanding of the stratigraphy of the basin. The

last stratigraphic subdivision proposed by Araujo and Nogueira (2019) is adopted in this work and is outlined in Figure 2. Relevant time constraints are presented in Figure 4 and Table 1.

The Itacaiúnas Supergroup consists of clastic, volcaniclastic and chemical sedimentary successions deposited during the Neoarchean and Paleoproterozoic and is usually divided into two groups, the Grão Pará Group at its base, which is subdivided into the Parauapebas and Carajás formations, and the Igarapé Bahia Group, which conformably overlies the Grão Pará Group. The Parauapebas Formation (Fig. 2), which unconformably overlies the basement rocks of the Carajás Domain, consists of basalts and basaltic andesites with minor pyroclastic rocks and rhyolites (Dardenne et al., 1988; Martins et al., 2017; Teixeira and Eggler, 1994). The age of Parauapebas Formation is well constrained between ca. 2770 and ca. 2750 Ma (Fig. 4, Table 1) by numerous U-Pb analyses on zircon grains extracted from volcanic rocks (Machado et al., 1991; Martins et al., 2017; Olszewski et al., 1989; Trendall et al., 1998; Wirth et al., 1986).

The base of the Carajás Formation is interlayered with volcanic rocks of the underlying Parauapebas Formation (Gibbs et al., 1986; Martins et al., 2017), showing the gradual and conformable contact between these two formations (Fig. 2). The Carajás Formation is mainly made up of banded iron deposits (Dalstra and Guedes, 2004; Klein and Ladeira, 2002; Tolbert et al., 1971) but also comprises minor black shales (Cabral et al., 2017), conglomeratic layers (Cabral et al., 2013), and iron formations containing stromatolitic features (Ribeiro da Luz and Crowley, 2012). The Carajás Formation is considered to have been deposited in a shallow marine platform (Ribeiro da Luz and Crowley, 2012). The age of deposition is fairly well constrained around 2745 Ma (U-Pb dating on zircon; Trendall et al., 1998; Fig. 4, Table 1). The Grão Pará Group has been suggested to correspond to a rift basin (Feio et al., 2012; Olszewski et al., 1989; Tavares et al., 2018; Toledo et al., 2019), possibly related to post-orogenic extension (Martins et al., 2017; Tavares et al., 2018).

The Igarapé Bahia Group (Fig. 2) forms the top of the Itacaiúnas Supergroup and comprises sandstone and siltstone interbedded with polymictic conglomerate containing angular clasts of BIF, cherts and volcanic rocks (Dreher et al., 2008, 2005; Galarza et al., 2008; Melo et al., 2019; Ronze et al., 2000). These sediments have been interpreted as turbiditic deposits (Dreher et al., 2008). Localized intense fluid circulation through the more permeable conglomeratic layers produced Au-Cu ore deposits (Dreher et al., 2008; Ronze et al., 2000; Tallarico et al., 2005). U-Pb dating of hydrothermal monazite indicates that fluid circulation occurred at 2575 $\pm$ 12 Ma (Tallarico et al., 2005), providing a minimum depositional age for this group. The age of the Itacaiúnas Supergroup (including the Igarapé Bahia Group) is further constrained by intrusive granitoids (Feio et al., 2013, 2012; Sardinha et al., 2006) giving a minimum age of 2735 $\pm$ 5 Ma (Feio et al., 2012; Fig. 4, Table 1).

The Serra Sul Formation (Fig. 2) comprises massive diamictites and polymictic conglomerates interbedded with fine-grained sediments, which have recently been interpreted as glaciogenic in origin (Fig. 2, Araújo and Nogueira, 2019). The arguments for a glaciogenic origin rely on the occurrence of foliated to massive diamictites, sandstone with micro-striated quartz grains, sometimes exhibiting outsized clasts and rhythmites made up of even parallel laminations (Araujo and Nogueira, 2019). Sedimentary rocks of the Serra Sul Formation are deformed and slightly metamorphosed, as testified by the occurrence of steep dipping beds, pressure shadows and foliation (Araujo and Nogueira, 2019).

The stratigraphic relationships of the Serra Sul Formation with other sedimentary units are poorly documented. The Serra Sul Formation overlies unconformably the Grão Pará Group (Araujo and Nogueira, 2019). Preliminary mapping results suggest that the Serra Sul Formation also unconformably overlies the Águas Claras Formation (Araújo Filho et al., 2020). Because the Águas Claras Formation is made up of slightly metamorphosed to unmetamorphosed

sandstones and siltstones (Pinheiro and Holdsworth, 1997), its appears paradoxical that this formation is covered by the metamorphosed and deformed Serra Sul Formation. Given the inherent difficulty to map the region, stratigraphic relationships inferred from the preliminary map of Araújo Filho et al. (2020) are here considered cautiously. The age of the Serra Sul Formation is poorly constrained between ca. 2740 Ma and ca. 1880 Ma (Fig. 4). A deposition between ca. 2575 Ma to ca. 2060 Ma has initially been proposed for the Serra Sul Formation (Araujo and Nogueira, 2019). However, this time interval relies on the mistaken interpretation made by Araújo and Nogueira (2019) that the 2575 $\pm$ 12 Ma age obtained on monazite from hydrothermal veins (Tallarico et al., 2005) and the poorly constrained 2.06-1.88 Ga age defined by Mougeot (1996, unpublished PhD thesis) represent depositional ages, although these dates were considered both by Tallarico et al. (2005) and Mougeot (1996) to represent the age of fluid circulation. Unclear stratigraphic relationships of the Serra Sul Formation with other units of the Carajás Basin and the absence of reliable radiochronologic age constraints require additional geochronological studies to infer the depositional age of the Serra Sul Formation.

3. Methodology

3.1. Sedimentological analyses and sampling

Four fully cored wells (GT12; GT13; GT16 and FD02) intercepting the Serra Sul Formation in the central part of the Carajás Basin (Fig. 3A and 3B) were examined in this study. About 1500 meters cumulated length of these drill cores (core diameter varies from 4.5 to 5 cm) were logged at the 1/100 scale to identify their sedimentary facies. The detailed sedimentological

characteristics of the different facies identified (i.e., lithology, sedimentary structures, petrography, clast lithology and shape, grading, syn-sedimentary deformational structures, nature of the bedding contacts between successive facies) were described. The results were then integrated to define facies associations and reconstruct depositional environments.

Thirteen samples were collected in the four drill cores for detrital zircon U-Pb dating. In order to evaluate if maximum depositional ages approximate true depositional ages, seven samples were collected along a single drill core (GT16) to assess whether maximum depositional ages are getting younger up-section (Rossignol et al., 2019). We also sampled different sedimentary facies to minimize potential bias associated with sediment transport mechanisms (Hietpas et al., 2011; Lawrence et al., 2011).

3.2. U-Pb zircon geochronology

3.2.1. Analytical methods

Zircon grains were extracted following a classical mineral separation procedure. Heavy minerals from <250 µm grain size fraction were successively concentrated by panning, hand magnet to remove the most magnetic minerals fraction, Frantz isodynamic magnetic separation, with Frantz settings kept below 1.8 A and 10° side-slope (Sircombe and Stern, 2002), and funnel separation in heavy liquid (methylene iodide). Zircon grains were then handpicked under a binocular microscope to produce the most representative sampling, with the aim to avoid intentional bias, even if some bias can be introduced by hand picking (Košler et al., 2013; Malusà et al., 2013; Sláma and Košler, 2012). After embedding the grains in an epoxy resin, the pucks were hand grounded to reveal equatorial cross sections. Laser

microsampling sites were chosen based on cathodoluminescence (CL) imaging by Scanning Electron Microscopy (SEM) using a JEOL 6510 equipped with a Centaurus cathodoluminescence detector.

To conduct *in situ* isotopic analyses, samples were ablated using a Photon machine G2 Excimer laser system connected to a ThermoFisher Scientific Element II Sector Field-Inductively Coupled Plasma-Mass Spectrometer. During the course of the analyses, the signals of ^{204}(Pb+Hg), ^{206}Pb, ^{207}Pb, ^{208}Pb, and ^{238}U masses were acquired. No common Pb correction was applied. The ^{235}U signal was calculated from ^{238}U using the ratio ^{235}U/^{238}U = 137.88. Laser spot diameters of 25 to 30 μm with repetition rates of 10 Hz were used for ablation. Every 14 unknown analyses were bracketed by two measurements of primary BB standard (Santos et al., 2017) followed by two measurement of secondary GJ-1 (Jackson et al., 2004) and Plesovice (Sláma et al., 2008) standards, to correct for mass fractionation and bias and to control data reproducibility, respectively.

When feasible, both cores and rims were analyzed (Zimmermann et al., 2018). A total of 1222 U-Pb analyses performed on 1197 grains were obtained, with a minimum of 12, and a maximum of 227 zircon grains analyzed per sample. Detailed analytical methods are presented in Appendix 2.

3.2.2. Data filtering, maximum age calculations and detection limits

A two-step procedure has been applied to calculate maximum depositional ages. The first step consisted in filtering the data based on their probability of concordance calculated using the relevant function in Isoplot/Ex 3.00 (decay constant errors included; Ludwig, 2012, 1998). Decay constant and decay constant errors are those of Steiger and Jäger (1977). The cut-off level applied to filter the data was 10% (e.g., Nemchin and Cawood, 2005; Rossignol et al.,

2016). In what follows, concordant analyses are those showing a probability of concordance ≥ 10%. Concordant analyses were then selected to calculate the maximum depositional age for each sample. To ensure a robust age estimate, we selected the youngest cluster of at least three grains overlapping at 2σ standard deviation (Coutts et al., 2019; Dickinson and Gehrels, 2009). Maximum depositional ages were calculated as the concordia age (Ludwig, 1998) of these youngest clusters using Isoplot/Ex 3.00 and are provided with 95% confidence limits. Hereafter quoted dates are concordia ages.

To assess the representativeness of the filtered data, the detection limits, that is the relative proportions of zircon population expressed as the percentage of the total population likely to remain undetected at a given confidence level (Andersen, 2005), are provided. Detections limits (DL), calculated following Andersen (2005) and Rossignol et al, (2016) are given for 1 (DL_1) and 3 (DL_3) grains at the 50 % (subscript $_{(pL=0.5)}$) and 95% (subscript $_{(pL=0.95)}$) confidence levels.

4. Sedimentary facies analysis

Nine facies (Table 2) were identified in the four drill cores (Fig. 5). Petrographic descriptions performed on representative samples of the main sedimentary facies are shown in Table 3. Sedimentary facies are grouped into three main facies associations (FA1, FA2 and FA3; Table 4), each of them corresponding to a specific depositional environment (Fig. 6). Representative conglomeratic facies, fine-grained, and syn-to post-depositional deformation structures are presented in Figs. 7, 8 and 9, respectively.

4.1. FA1: polymictic conglomerate interbedded with sandstone and siltstone

Description. FA1 comprises polymictic conglomerates (facies G1, Table 2) interbedded with sandstones (facies S1, Table 2) and fine-grained sediments (facies F1 and F2, Table 2). These different facies are described below.

Facies G1 represents the dominant lithology in the drill core GT12 and a significant part of other drill cores (Fig. 5). G1 facies consists of thick (up to tens of meters) massive or normally graded conglomeratic beds. The basal contact of G1 beds is generally sharp, slightly or non-erosive, while the upper contact is often diffuse, progressively evolving from sandstone to siltstone facies (Fig. 7A). The conglomerates are clast to matrix supported (Fig. 7B and 7C), polymictic and rather poorly sorted, with clast size ranging from mm to tens of cm. The clasts show a wide variety of lithologies (metamorphic, magmatic and sedimentary; Table 3; e.g., sample GT16 134.20), shapes (from rounded to angular) and sphericity (from nearly spherical to very elongated; Fig. 7A, C). The clasts are generally randomly oriented (Fig. 7A and 7B), but a few beds contain well-oriented clasts (Fig. 7C). The matrix is sandy to silty and comprises a wide variety of minerals and lithic fragments (Table 3; e.g., sample GT16 130.25).

Facies S1 is present in all drill cores (Fig. 5) and occurs either as individual beds with sharp contacts or overlying G1 facies beds with diffuse contact. The Facies S1 consists of medium-grained sand to gravel and commonly contains floating clasts (Fig. 8A and 8B) and diagenetic pyrite (Fig. 8C). Petrographic observations indicate that these sandstones are mainly made up of lithic fragments (cherts and polycrystalline quartz grains) and monocrystalline quartz grains (Table 3; e.g., sample GT16 102.20).

Facies F1 and F2 consist of fine-grained sediments (fine sandstone to siltstone and clay) defining horizontal laminations (Fig. 8C) underlined by thin sandstone layers. Small current ripples forming sandy lenses within the silt to clay sediments are locally present (Fig. 8D) and

are sometimes reworked by wave ripples at their top. A few coarser beds, generally normally graded, are interbedded within F1 and F2 facies (Fig. 8E). Siltstones are greyish (F1) to blackish (F2, black shales) reflecting various organic carbon contents.

In all drill cores, FA1 shows evidence for both syn- to post-depositional deformation features (Fig. 9). Syn-depositional deformation features include (*i*) isolated folds indicative of slumping processes (Fig. 9A), (*ii*) convoluted laminations well preserved in the fine-grained facies (F1, F2) (Fig. 9B), (*iii*) small clastic dykes consisting of fine-grained sediments injected between and through other sediments (Fig. 9C), (*iv*) flame structures, load casts or water escape figures at the contact between coarse sandstone and finer siltstone layers (Fig. 9D) and (*v*) cm-scale syn-sedimentary faults cutting across fine-grained sediments (Fig. 9E). In addition, soft sediment deformation can affect adjacent sedimentary facies (coarse and fine sands, gravels, pebbles). Owing to their competency contrasts, deformation in these domains often result in the buckling of the incompetent fine sandstone layers around more competent pebbles (Fig. 9F).

Interpretation. G1 facies represents deep water sediments deposited by subaqueous mass flow, cohesive debris flow or hyper-concentrated density flow (Lowe, 1982; Mulder and Alexander, 2001; Nemec and Steel, 1984; Postma et al., 2014; Postma and Cartigny, 2014; Walker, 1975). The polymictic nature of the conglomerates is best attributed to the mixing of materials of different origins during downslope debris flow (Eyles and Eyles, 2000). G1 conglomerates are commonly capped by sandy deposits (S1) containing floating clasts (gravels to pebbles), which are interpreted as sub-aqueous debris flow deposits evolving toward high-density turbidity currents (Nemec and Steel, 1984) or rapid suspension fallout (Postma, 1990). F1 and F2 facies are indicative of deposition from suspension (silt and clay), sometimes with

organic matter (F2 facies), from waning turbidity currents. The starved current ripples forming small sandy lenses within the silty to clayey deposits are interpreted to be produced by traction from low concentration turbidity currents. The numerous syn- to post-depositional deformations occurring within these sedimentary facies are also consistent with deep-water environments (e.g., Ducassou et al., 2019; Ravier et al., 2015; Rubi et al., 2018). Abundant load casts and fluid escape structures suggest rapid deposition from short-lived flows (i.e., subaqueous mass flow, cohesive debris flow, or hyper-concentrated density flow). The common occurrence of syn-sedimentary small faults in the laminated fine sandstones and siltstones, with mm to cm throws, is interpreted to reflect mass-movement of sediments on a slope (Collinson, 1994), pointing to deep marine environment (Fig. 6). Injectites are also common features of deep sea fan deposits (e.g., Archer, 1984; Ravier et al., 2015).

4.2. FA2: flat pebbles conglomerate and slumped deposits

Description. FA2 comprises flat pebbles conglomerates (facies G2, Table 2) interbedded with polymictic conglomerates (facies G1), massive (facies S1) and chaotic and disordered sandstone horizons (facies S2, Table 2). Facies G1 and S1 are described above. Facies G2 and S2 represent two facies of minor extent, which were identified in three out of four drill cores (GT13, GT16, and FD02, Fig. 5).

Facies G2 is a conglomeratic facies made up of intraclastic granules to pebbles consisting of fine sand, silt to clay, or laminated fine sand and silt. These conglomerates are matrix to clast-supported, and some clasts exhibit a stratification (Fig. 7D), display an elongated and sub-rounded to rounded shape (Fig. 7E, 7F), or exhibit ductile deformation (Fig. 7G). The matrix comprises rounded to sub-angular monocrystalline quartz and chlorite

embedded within silty material (Table 3; sample GT16 296.20). Zircon is present as an accessory mineral.

Facies S2 comprises mainly sand and silt, but also a few coarser-grained sediments, including pebble-sized clasts. This facies is characterized by chaotic beds, where the initial lamination is either disordered, folded, sheared or sometimes not recognizable.

Interpretation. The G2 facies is interpreted to result from the failure and subsequent reworking of compacted to loosely consolidated shoreface deposits (Myrow et al., 2004). The occurrence of finely laminated features preserved in individual flat pebbles argues for limited transport by mass movement in relatively shallow water environments (shoreface to upper offshore). Rupture could have been induced by storm or seismic waves indicative of an energetic environment. Downslope movements of mainly fine-grained sediments producing chaotic bedding can best explain S1 and S2 facies (Martinsen, 1994). Facies G2 is commonly interbedded with G1 facies conglomerate suggesting different degrees of mixing of various materials during slumping and subsequent sediment gravity flow processes (Eyles and Eyles, 2000). The facies forming FA2 are indicative of relatively shallow subaqueous environments characterized by slope instability, slumping and gravity flow processes (Fig. 6).

4.3. FA3: fine-grained sediments with microbial deposits

Description. FA3 comprises fine-grained siliciclastic (facies F1, F3 and S2; Table 2) and carbonaceous-rich facies (facies M1 and M2; Table 2). This facies association has been identified in drill core FD02 only (Fig. 5). Facies F1 and S2 are described above.

Facies F3 and M1 occur in close association as alternate domains and are therefore described together. Facies F3 consists of greyish, fine to medium sandstone alternating with

silt beds and exhibits current ripples and wave ripples. Facies M1 is made up of very fine, mm-thick, crinkly- to wrinkly-laminated features that are rhythmically organized in cm-thick domains (Fig. 8F). Facies M2 consists of a single 15 cm thick bed localized at about 400 m depth at the base of drill core FD02 (Fig. 5). This bed comprises dark, likely organic-rich matter, clotted, elongated masses of a few mm to cm long, which display diffuse boundaries and a preferred orientation parallel to the stratigraphic plane (Fig. 8G). These small elongated masses occur embedded in a greyish silty to clayish matrix containing secondary pyrite mineralization.

Interpretation. The occurrence of wave ripples in the fine sandstones and siltstones indicates a shallow subaqueous environment subjected to fair weather wave action. Crinkly to wrinkly laminations in terrigenous sediments are common criteria of microbial mats (Hagadorn and Bottjer, 1997). Microbial mats commonly develop in the photic zone within a few meters from the surface under low turbid conditions indicative of low energy environments, which is in agreement with the presence of sedimentary structures such as wave ripples (Fig. 6). Facies M2 is more enigmatic and the occurrence of clotted dark masses is tentatively interpreted as reworked microbial mats.

5. Geochronological constraints

Cathodoluminescence (CL) images of representative grains are presented in Fig. 10, and concordant results are presented in Fig. 11 according to their stratigraphic location in the drill cores, from the older to the younger. Description of the zircon typography for each sample is

presented in Appendix 3, analytical results in Appendix 4, and geochronological diagrams for each sample including both concordant and discordant analyses in Appendix 5.

GT16 296.14-296.32. Seventy-six grains extracted from this flat pebble conglomerate gave concordant dates, resulting in detection limits ranging from 0.9% for the $DL_{1(pL=0.5)}$ to 8.0% for the $DL_{3(pL=0.95)}$ (Table 5). In CL, most of the grains display a well-defined oscillatory zoning (Fig. 10A) typical of magmatic zircon (e.g., Corfu et al., 2003; Shore and Fowler, 1996). The Th/U ratios of concordant grains range between 0.47 and 2.49 (Appendix 4), also supporting a magmatic origin (e.g., Rubatto, 2002), even if metamorphic grains can have similar Th/U ratios (e.g., Kelly and Harley, 2005; Teipel et al., 2004).

The youngest cluster, defined by 10 grains (10 analyses), gives a concordia date of 2770.1 ± 8.9 Ma (MSWD = 0.67, probability of concordance and equivalence = 0.85; Table 5), interpreted as the maximum depositional age for this conglomerate (Fig. 11A). Other concordant dates spread from the maximum depositional age up to the mid Mesoarchean, at 3058 ± 25 Ma.

GT16 295.85-296.07. Thirty-three grains from this sample are concordant and give detection limits ranging from 2.1% for the $DL_{1(pL=0.5)}$ to 17.9% for the $DL_{3(pL=0.95)}$ (Table 5). In CL, most grains display a well-defined oscillatory zoning typical of magmatic zircon, but a few grains exhibit a faint and patchy brightness (Fig. 10B). The Th/U ratios of concordant grains range between 0.38 and 2.41, also supporting a magmatic origin.

The youngest cluster, defined by 5 grains (5 analyses), gives a concordia date of 2786 ± 12 Ma (MSWD = 1.5, probability = 0.13; Table 5), interpreted as the maximum depositional

age for this conglomerate (Fig. 11A). Other concordant dates spread from the maximum depositional age up to the Paleoarchean, at 3238 ± 27 Ma.

GT16 279.96-280.09. This sandstone yielded 67 concordant grains, giving detection limits ranging from 1.0% for the $DL_{1(pL=0.5)}$ to 9.1% for the $DL_{3(pL=0.95)}$ (Table 5). Most of the grains display a well-defined oscillatory zoning (Fig. 10C) and have Th/U ratios ranging between 0.36 and 4.08, supporting a magmatic origin.

The youngest cluster, defined by 7 grains (7 analyses), gives a concordia date of 2718 ± 12 Ma (MSWD = 0.95, probability = 0.50; Table 5), interpreted as the maximum depositional age for this conglomerate (Fig. 11A). Other concordant dates spread from the maximum depositional age up to the early Mesoarchean, at 3161 ± 29 Ma.

GT16 250.40-250.55. Twenty-two zircon minerals from this polymictic conglomerate are concordant, giving detection limits ranging from 3.1% for the $DL_{1(pL=0.5)}$ to 26.0% for the $DL_{3(pL=0.95)}$ (Table 5). In CL, most of the grains display a well-defined oscillatory zoning typical and sometimes contain inclusions of other minerals (Fig. 10D). The Th/U ratios of concordant grains range between 0.43 and 3.42, corroborating a magmatic origin.

The youngest cluster, defined by 4 grains (4 analyses), gives a concordia date of 2767 ± 14 Ma (MSWD = 0.94, probability = 0.47; Table 5), interpreted as the maximum depositional age for this conglomerate (Fig. 11A). Most of the other concordant dates spread from the maximum depositional age up to the mid Mesoarchean, at 3034 ± 26 Ma. One grain yielded a concordant date of 2698 ± 26 Ma, suggesting that the deposition of the sediment could have been younger that the preferred maximum depositional age. However, because only one concordant grain gives a date of ca. 2698 Ma and as no separate aliquot has been analyzed to

test reproducibility, the statistical requirements are not met to confidently consider this date as a maximum depositional age.

GT16 174.29-174.45. Fifty-two grains from this coarse sandstone are concordant, giving detection limits ranging from 1.3 % for the $DL_{1(pL=0.5)}$ to 11.7% for the $DL_{3(pL=0.95)}$ (Table 5). Most of the grains display a well-defined oscillatory zoning, and some grains contain mineral inclusions (Fig. 10E). The Th/U ratios of concordant grains range between 0.42 and 2.72, also supporting a magmatic origin.

The youngest cluster, defined by 10 grains (10 analyses), gives a concordia date of 2708 ± 11 Ma (MSWD = 0.67, probability = 0.85; Table 5), interpreted as the maximum depositional age for this conglomerate (Fig. 11A). Other concordant dates spread from the maximum depositional age up to 2979 ± 32 Ma.

GT16 140.51-140.65. Twenty-two grains from this conglomerate are concordant, giving detection limits ranging from 3.1% for the $DL_{1(pL=0.5)}$ to 26.0% for the $DL_{3(pL=0.95)}$ (Table 5). In CL, some grains display a well-defined oscillatory zoning typical of magmatic zircon, while other grains have more complex internal structures, showing resorption features, rather commonly observed in magmatic zircon (Fig. 10F). The Th/U ratios of concordant grains range between 0.11 and 3.03, also supporting a magmatic origin.

The youngest cluster, defined by 5 grains (5 analyses), gives a concordia date of 2748 ± 12 Ma (MSWD = 0.65, probability = 0.75; Table 5), interpreted as the maximum depositional age for this conglomerate (Fig. 11A). Other concordant dates spread from the maximum depositional age up to 3060 ± 26 Ma.

GT16 134.15-134.45. This polymictic conglomerate yielded 77 concordant grains, giving detection limits ranging from 0.9% for the $DL_{1(pL=0.5)}$ to 8.0% for the $DL_{3(pL=0.95)}$ (Table 5). The grains display a well-defined oscillatory zoning (Fig. 10G) and have Th/U ratios ranging between 0.41 and 4.25, supporting a magmatic origin.

The youngest cluster, defined by 10 grains (10 analyses), gives a concordia date of 2815.8 ± 8.8 Ma (MSWD = 1.40, probability = 0.12; Table 5), interpreted as the maximum depositional age for this conglomerate (Fig. 11A). Most of the other concordant dates spread from the maximum depositional age up to the Paleoarchean, at 3345 ± 27 Ma. One grain yielded a concordant date of 2749 ± 27 Ma, suggesting that the deposition of the sediment could have been younger than the preferred maximum depositional age, but statistical requirements are not met to confidently consider this date as a maximum depositional age.

GT13 213.85-214.00. This feldspathic wacke (Table 3) yielded 32 concordant grains, resulting in detection limits ranging from 2.1% for the $DL_{1(pL=0.5)}$ to 18.4% for the $DL_{3(pL=0.95)}$ (Table 5). In CL, some grains display a well-defined oscillatory zoning typical of magmatic zircon, and some contain mineral inclusions, suggesting a magmatic origin (Fig. 10H), also supported by Th/U ratios ranging between 0.49 and 2.29.

The youngest cluster, defined by 4 grains (4 analyses), gives a concordia date of 2674 ± 17 Ma (MSWD = 1.5, probability = 0.17; Table 5), interpreted as the maximum depositional age for this sample (Fig. 11A). Other concordant dates spread from the maximum depositional age up to 2998 ± 29 Ma.

GT13 211.95-212.15. This quartz wacke yielded 54 concordant grains, corresponding to detection limits ranging from 1.3% for the $DL_{1(pL=0.5)}$ to 11.3% for the $DL_{3(pL=0.95)}$ (Table 5). Some

grains display a well-defined oscillatory zoning, and other exhibit a core and rim structure (Fig. 10I). The Th/U ratios of concordant grains range between 0.24 and 3.21, also supporting a magmatic origin.

The youngest cluster, defined by 10 grains (10 analyses), gives a concordia date of 2701.6 ± 9.2 Ma (MSWD = 0.40, probability = 0.99; Table 5), interpreted as the maximum depositional age for this sample (Fig. 11A). Other concordant dates spread from the maximum depositional age up to 2976 ± 27 Ma.

*GT13 200.50-200.*65. Only two grains from this sandstone are concordant, giving very high detection limits of 29.3% for the $DL_{1(pL=0.5)}$ and 77.6% for the $DL_{1(pL=0.95)}$ (Table 5). The grains display a well-defined oscillatory zoning (Fig. 10J) and have Th/U ratios ranging between 1.42 and 3.39, supporting a magmatic origin.

The two concordant grains do not allow to calculate a maximum depositional age following robust statistical criterions. Thus, the concordia date of 2947 ± 23 Ma (MSWD = 0.34, probability = 0.80; Table 5; Fig. 11A) is only considered as a preliminary results and no further interpretation is provided for this sample.

*GT13 185.95-186.*15. Only 11 concordant were recovered in this sandstone, giving high detection limits ranging from 6.3% for the $DL_{1(pL=0.5)}$ to 47.1% for the $DL_{3(pL=0.95)}$ (Table 5). In CL, some grains display a well-defined oscillatory zoning typical of magmatic zircon. Some grains exhibit a core surrounded by overgrowth (Fig. 10K). The Th/U ratios of concordant grains range between 0.56 and 4.31, also supporting a magmatic origin.

The youngest cluster, defined by 8 grains (8 analyses), gives a concordia date of 2706 ± 12 Ma (MSWD = 0.61, probability = 0.87; Table 5), interpreted as the maximum depositional age for this sample (Fig. 11A). Three other concordant dates are grouped around 2850 Ma.

*GT12 353.40-353.*70. Only 12 concordant were recovered in this polymictic conglomerate, giving high detection limits ranging from 5.6% for the $DL_{1(pL=0.5)}$ to 43.9% for the $DL_{3(pL=0.95)}$ (Table 5). In CL, some grains display a well-defined oscillatory zoning and sometimes exhibit a core and rim structure (Fig. 10L). The Th/U ratios of concordant grains range between 0.76 and 2.33, also supporting a magmatic origin.

The youngest cluster, defined by 9 grains (9 analyses), gives a concordia date of 2821.3 ± 9.3 Ma (MSWD = 0.76, probability = 0.74; Table 5), interpreted as the maximum depositional age for this sample (Fig. 11A). Two other concordant dates are older and give date of 2882 ± 25 Ma and 2952 ± 25 Ma. Another grain yielded a concordant date of 2741 ± 36 Ma, suggesting that the deposition of the sediment could have been younger that the preferred maximum depositional age, but statistical requirements are not met to confidently consider this date as a maximum depositional age.

*FD02 118.80-119.*15. Eleven concordant were recovered in this coarse sandstone, giving high detection limits ranging from 5.2% for the $DL_{1(pL=0.5)}$ to 41.3% for the $DL_{3(pL=0.95)}$ (Table 5). The grains display a well-defined oscillatory zoning and sometimes exhibit a core and rim structure (Fig. 10M). The Th/U ratios of concordant grains range between 0.46 and 1.29, also supporting a magmatic origin.

All the grains form a single cluster (13 grains, 14 analyses) giving a concordia date of 2722.8 ± 8.3 Ma (MSWD = 0.58, probability = 0.96; Table 5), interpreted as the maximum depositional age for this sample (Fig. 11A).

6. Discussion

6.1. Paleoenvironments of the Serra Sul Formation

Polymictic conglomerates represent one of the main sedimentary facies of the Serra Sul Formation (Fig. 5). They consist of poorly sorted conglomerates, which fits well the definition of “diamictite”. Diamictites can be produced in a wide range of depositional settings (Eyles and Januszczak, 2004). In particular, polymictic and poorly sorted conglomerates are common in subaqueous environments subjected to recurrent sedimentary input originating from an upward slope and deposited through gravity processes (e.g., Ducassou et al., 2019; Kim et al., 1995; Lenhardt et al., 2011; Nemec and Steel, 1984; Rohais et al., 2008; Walker, 1975). The association between fine sandstone to siltstone, comprising horizontal laminations (Fig. 8C) and starved ripples marks (Fig. 8D) and poorly sorted conglomerates shows that waning sub-aqueous debris flow evolved toward turbidity current followed by deposition of silt particle by suspension (Nemec and Steel, 1984).

The poorly sorted conglomerates and some associated sandstones frequently host outsized clasts (Fig. 8B). Such outsized clasts are common in sediments deposited by gravity processes (e.g., Kim et al., 1995; Lenhardt et al., 2011; Nemec and Steel, 1984; Postma et al., 2014; Rohais et al., 2008; Rubi et al., 2018). In the Serra Sul Formation, outsized clasts occur in sandstones associated with conglomerates deposited by gravity processes.

The sediments from the Serra Sul Formation are marked by numerous syn-sedimentary faults (e.g., Fig. 9E) and are cut across by clastic injections (e.g., Fig. 9C) indicative of fluid overpressure (e.g., Dubois et al., 2017). These processes are known to enhance dissolution and produce micro-striations (Arnaud and Etienne, 2011; Atkins, 2004) and fit well with the report of micro-striations on quartz grains (Araujo and Nogueira, 2019).

Additional distinctive features of the Serra Sul Formation include microbially-mediated sedimentary structures (Fig. 8F) associated with wave generated ripples. These microbially-mediated sedimentary structures typically formed in the photic zone under low turbid conditions (Hagadorn and Bottjer, 1997; Vennin et al., 2015).

The various facies and their associations points to a subaqueous landscape with developed microbial activity in shoreward settings and instable slope settings downward, where gravity flow processes reworked siliciclastic sediments (Fig. 6). Despite recent suggestion that the sediments from the Serra Sul Formation are of glacial origin and were derived either from glacier ice (tillites) or periglacial processes (Araujo and Nogueira, 2019), no glacial influence is required to explain the deposition of these sedimentary rocks. Importantly, the presence of wave generated ripples associated with microbialites even argue against the occurrence of a perennial ice cover inhibiting wave generation (Williams et al., 2016). The fact that no glacial influence is required do not rules out that a glacial influence actually existed. For instance, it cannot be excluded that the poorly sorted conglomerates represent glaciogenic sediments temporarily stored on an unstable margin and later redeposited through gravity processes (Eyles and Januszczak, 2004). However, in the light of presently available evidences, a glacial influence represents an unnecessary hypothesis to account for all observations made in the Serra Sul Formation. Until more compelling evidence pointing to a glacial setting are found, such as striated pavement and pebbles (Arnaud and

Etienne, 2011), we favor a simpler paleoenvironmental interpretation for the Serra Sul Formation, with developed microbial activity in shoreward settings and instable slope settings downward (Fig. 6).

6.2. Age and provenance of the Serra Sul Formation

6.2.1. Age of the Serra Sul Formation

Our petrographic investigations (Table 3) show the occurrence of volcaniclasts as a minor component of the polymictic sandstones and conglomerates of the Serra Sul Formation. In addition, different magmatic events have been documented in the Carajás Basin or in its vicinity at ca. 2.75 Ga (Machado et al., 1991; Martins et al., 2017; Olszewski et al., 1989; Trendall et al., 1998; Wirth et al., 1986), ca. 2.70 Ga (Melo et al., 2017) ca. 2.5 Ga (Toledo et al., 2019). The occurrence of protracted magmatic activities in and around the Carajás Basin constitutes a favorable circumstance to obtain maximum depositional ages approximating the age of sedimentation (Cawood et al., 2012; Sharman and Malkowski, 2020). To test this hypothesis, we collected seven samples along a single drill core (GT16, sample location in Fig. 5) to verify if maximum depositional ages become younger up-section.

Because volcaniclastic rocks can contain several zircon populations (e.g., Rossignol et al., 2019), a large number of zircons were analyzed in each sample to ensure that the main populations were sampled and effectively dated. For the seven samples collected along drill-core GT16, the detection limits range from 0.9% for the $DL_{1(pL=0.5)}$ to 26.0% for the $DL_{3(pL=0.95)}$ (Table 5). With the exception of two samples out of seven that show slightly higher detection limits, these overall small detection limits minimized the risk of missing important zircon

populations. We also minimized potential hydraulic bias (Hietpas et al., 2011; Lawrence et al., 2011) by selecting rock sample with different grain sizes (Table 3).

The seven samples collected along drill-core GT16 yield maximum depositional ages that are not getting younger up-section, but rather appear uncorrelated to their stratigraphic position in the drill core (Figs. 5 and 11A). This is likely due to maximum depositional ages calculated from zircon populations that are not deriving from volcanic, autocrystic, zircon grains that crystallized contemporaneously to the sedimentation (Rossignol et al., 2019). The youngest maximum depositional age obtained in the Serra Sul Formation is given by sample GT13 213.85-214.00, indicating that the deposition is younger than 2674 ± 17 Ma. Assuming the youngest grains present in different samples of the Serra Sul derive from a single, cogenetic source, as suggested by their homogeneous Th/U ratio (1.69 ± 0.46), gives a slightly more precise maximum depositional date of 2684 ± 10 Ma (n = 10, MSWD = 0.62, probability = 0.89; Fig. 11B; Table 5). This date, which is similar but slightly more precise than the maximum depositional age obtained for sample GT13 213.85-214.00 (Fig. 11A), is interpreted as the maximum depositional age for the Serra Sul Formation.

Although the contact between the Serra Sul Formation and A-type granitoids of the Uatumã Silicic Large Igneous Province has never been observed, the latter intrudes the whole Carajás sedimentary succession, probably including the Serra Sul Formation, and might provide an upper bound age for this formation. Close to the area where the Serra Sul Formation is exposed, the Serra dos Carajás Granite (Fig. 3B) has an age of 1880 ± 2 Ma (Machado et al., 1991). Consequently, the Serra Sul Formation can have been deposited at any time between 2684 ± 10 Ma and 1880 ± 2 Ma.

6.2.2. Provenance analysis and potential stratigraphic implications

The age distribution of the Serra Sul Formation is polymodal (Fig. 12), with major peaks at ca. 2715 Ma, 2790-2830 Ma, 2930 Ma, 2990 Ma and 3050 Ma. Such polymodal distribution is fully consistent with the diversity of zircon types evidenced by CL imaging (Fig. 10) and the polymictic nature of the sandstones and conglomerates (Table 3).

The ca. 3050 Ma population likely derived from the oldest rocks forming the basement of the Carajás Domain, characterized by protolith ages of ca. 3080 to ca. 3000 Ma (Machado et al., 1991; Moreto et al., 2015; Pidgeon et al., 2000). The ca. 2990 Ma population match the age of the ca. 2980 TTG suites of the Rio Maria Domain (Almeida et al., 2013). Because the Rio Maria and Carajás domains collided by the end of the Mesoarchean, the ca. 2990 Ma population of the Serra Sul Formation likely derived, either directly or after sedimentary recycling, from the Rio Maria Domain. The ca. 2930 Ma population corresponds to the age of the ca. 2960 Ma to ca. 2930 Ma TTG forming the basement of the Carajás Basin (Feio et al., 2013). A local TTG source is thus likely for this ca. 2930 Ma zircon population. A broad peak in age distribution is plateauing between ca. 2790-2830 Ma (Fig. 12). This broad peak partially matches the age of the last TTG magmatic episode documented in the basement of the Carajás Basin, that ended around 2830 Ma (Feio et al., 2013; Machado et al., 1991; Moreto et al., 2015; Pidgeon et al., 2000). The 2790-2830 Ma peak also partially matches the age of a volcaniclastic succession that was deposited at 2774 ± 19 Ma to the north of the Carajás Domain (Toledo et al., 2019). Thus, the 2790-2830 Ma peak in age distribution might correspond to two populations, deriving from local TTG and volcaniclastic sources located in the Carajás Domain. The most important peak in age distribution, around 2715 Ma, corresponds to the age of a magmatic event that occurred at 2701 ± 30 Ma in the Carajás

Domain (Melo et al., 2017). This suggests that the ca. 2715 Ma detrital population also has a local source.

All the provenances of zircon grains present in the Serra Sul Formation originate from local sources that form the basement of the Carajás Basin. Only one population seems to derive from the southward Rio Maria Domain, which was already merged with the Carajás domain at the time of deposition of the Serra Sul Formation (Tavares et al., 2018). These local sources point to drainage networks limited to the Carajás Domain. It is noticeable that while these drainage networks virtually sampled all Archean magmatic rocks reported up to now in the Carajás Domain, except those corresponding to the ca. 2.5 Ga granite (Toledo et al., 2019). Such an absence can be explained by the fact that the ca. 2.5 Ga granite was not exposed and available for erosion at the time of deposition of the Serra Sul Formation, or that drainage networks did not sample this granite. A sampling bias could also account for the absence of such ca. 2.5 Ga old zircon population in the dataset obtained in this study, especially if this population represented less than 3.8% of all zircon grains present in the Serra Sul Formation (i.e., the lowest $DL_{1(pL=0.95)}$ obtained for a single sample; Table 5). Another hypothesis to explain the absence of such ca. 2.5 Ga population is that the Serra Sul Formation is actually older than 2.5 Ga. Such hypothesis is corroborated by strong similarities of sedimentary facies of the Serra Sul Formation with those of the Igarapé Bahia Group, which also comprises sandstone and siltstone interbedded with polymictic conglomerate containing angular clasts of BIF, cherts and volcanic rocks (Dreher et al., 2008, 2005; Galarza et al., 2008; Melo et al., 2019; Ronze et al., 2000). Contrarily to the Serra Sul Formation, the Igarapé Bahia Group is rather well dated and is older than 2575 $\pm$ 12 Ma (Tallarico et al., 2005). Because too limited sedimentological investigations are available to compare the Serra Sul Formation and the Igarapé Bahia Group, and because non unique interpretation can be made about the absence

of ca. 2.5 Ga zircon population in the Serra Sul Formation, we consider that the Serra Sul Formation can have been deposited at any time between ca. 2684 Ma and ca. 1880 Ma.

6.3 Implications for the tectonic evolution of the Amazonian Craton and large-scale correlations

The large time interval of ca. 800 Ma during which the Serra Sul Formation can have been deposited makes any correlation with other sedimentary units across the world speculative, and we restrict the following discussion to first order tectonic scenarios that compares with those of other cratons. The maximum depositional age of the Serra Sul Formation (2684 ± 10 Ma) demonstrates that it is significantly younger than the underlying Grão Pará Group, which was deposited before 2735 ± 5 Ma (Feio et al., 2012). This indicates a stratigraphic hiatus of at least 36 Ma (and likely much longer) between the end of the deposition of the Grão Pará Group and the deposition of the Serra Sul Formation (Fig. 13). The significance of this unconformity is speculative, but some characteristic features of the Serra Sul Formation points toward an unconformity related to an extensional tectonic phase. Coarse-grained sediments and numerous sedimentary features such as load casts attest for high sedimentation rates that commonly characterize rift settings. Depositional environments of the Serra Sul Formation, characterized by slope instability and gravity flow processes, are consistent with those usually encountered in active extensional settings (Gawthorpe and Leeder, 2000). In addition, the occurrence of various local sources shown by detrital zircon provenance analysis is in line with numerous small transverse drainage divides characterizing rift basins (Gawthorpe and Leeder, 2000). It is worth noting that a rift setting has also been proposed for the deposition of the underlying Grão Pará Group (e.g., Machado et al., 1991; Martins et al., 2017; Olszewski et al., 1989; Toledo et al., 2019). Together, sedimentary facies, depositional

environments, provenance of zircon grains as well as the rift setting attributed to the Grão Pará Group, suggest that this unconformity may have resulted from an ongoing extensional tectonic phase that affected the eastern Amazonian Craton (Carajás Province) during the late Neoarchean to early Paleoproterozoic.

The age of the rifting event in the eastern Amazonian Craton broadly coincides in time with the break-up of one of the first documented supercontinent (Eriksson and Condie, 2014; Pesonen et al., 2003; Reddy and Evans, 2009; Salminen et al., 2019; Fig. 13). For instance, continental rifting affected the Pilbara Craton during the Neoarchean, around 2.7 Ga (Blake, 1993). The onset of rifting in the Kaapvaal Craton also occurred during the course of the Neoarchean, at ca. 2.68 Ga (Olsson et al., 2010). In the São Francisco, Karelian-Kola and Superior cratons, rifting events initiated around the Neoarchean-Paleoproterozoic boundary, at ca. 2.50 Ga (Alkmim and Martins-Neto, 2012; Amelin et al., 1995; Ernst and Bleeker, 2010). The Neoarchean to Paleoproterozoic tectonic setting of the eastern Amazonian Craton compares with those documented in other major cratons across the world, and could record the break-up of one of the first documented supercontinent (Gumsley et al., 2017; Salminen et al., 2019). Such hypothesis is however speculative as the location of the Amazonian Craton during the Neoarchean and the Paleoproterozoic remains unknown. If correct, this suggests that the eastern Amazonian Craton could have been part of the proposed Supervaalbara supercontinent during the Archean, along with the São Francisco, Superior, Wyoming, Kola and Karelia, Zimbabwe, Kaapvaal, Tanzania, Yilgarn, and Pilbara cratons (Salminen et al., 2019).

7. Conclusions

The Serra Sul Formation was deposited in various subaqueous environments ranging from shallow to deep water settings. Shallow water environments are characterized by local occurrences of microbially-mediated structures. Deep water environments are characterized by polymictic conglomerates resulting from the mixing of materials of different origins during downslope debris flow. Provenance analysis based on detrital zircon age distribution indicates local origins, corresponding to various magmatic rocks forming the basement of the Carajás Basin.

Detrital zircon U-Pb dating indicates a maximum depositional age of 2684 ± 10 Ma for the Serra Sul Formation. This demonstrates that the Serra Sul Formation is significantly younger than the underlying Grão Pará Group, thus contributing to improve the stratigraphic framework of the Carajás Basin during the late Neoarchean to early Paleoproterozoic. We suggest here that the Serra Sul Formation and underlying Grão Pará Group were deposited during successive extensional tectonic phases that affected the Amazonian Craton during the late Neoarchean and the early Paleoproterozoic. The age of this rifting event broadly compares with those documented in various cratons across the world and could thus be related to the break-up of one of the first documented supercontinent.

Acknowledgements

This research was funded by grants of the Fundação Amparo à Pesquisa do Estado de São Paulo (FAPESP; 2015/16235-2; 2018/02645-2; 2018/14617-3, 2018/05892-0; 2019/17732-0, 2019/16066-7 and 2019/12132-5), the Conselho Nacional de Desenvolvimento Científico e Tecnológico (CNPq; 308045/2013-0 and 307353/2019-2), and the Fundação Amparo à

Pesquisa do Minas Gerais (FAPEMIG projet APQ-03793-16). José Pereira, Debora Vasconcelos and Ana Alkmim of the Universidade Federal de Ouro Preto are acknowledged for assistance during sample preparation and data acquisition. We acknowledge Sergio R. B. Huhn (formerly Vale company, now professor at the Federal University of Ceará, Brazil) for his help to access the Vale's drill core library in Carajás. Cathodoluminescence images of the zircon grains analyzed during this study were obtained by the Microscopy and Microanalysis Laboratory (LMic) of the Universidade Federal de Ouro Preto, a member of the Microscopy and Microanalysis Network of Minas Gerais State/Brazil/FAPEMIG. We acknowledge two anonymous reviewers for their constructive comments and suggestions that helped to clarify this manuscript.

Data Availability

Datasets related to this article can be found at https://data.mendeley.com/datasets/dmfn8gb4sg/draft?a=9a2279f2-b12b-4e1f-8fd3-1e2e41f2cb5b, an open-source online data repository hosted at Mendeley Data.

Author Contributions

C.R.: conceptualization, formal analysis, investigation, writing, visualization; E.S.R.: conceptualization, investigation, writing; F.N.: conceptualization, investigation, writing; L.T.: conceptualization, investigation, writing; J.N.A.: conceptualization, investigation, writing; M.A.L.S.: formal analysis, investigation, resources; C.L.: formal analysis, investigation, resources; P.P.: conceptualization, investigation, project administration, supervision, writing.

References

Alkmim, F., Martins-Neto, M.A., 2012. Proterozoic first-order sedimentary sequences of the Sao Francisco craton, eastern Brazil. Marine and Petroleum Geology 33, 127–139. https://doi.org/10.1016/j.marpetgeo.2011.08.011

Almeida, J.A.C., Dall'Agnol, R., Leite, A.A.S., 2013. Geochemistry and zircon geochronology of the Archean granite suites of the Rio Maria granite-greenstone terrane, Carajás Province, Brazil. Journal of South American Earth Sciences 42, 103–126. https://doi.org/10.1016/j.jsames.2012.10.008

Althoff, F., Barbey, P., Boullier, A.M., 2014. 2.8-3.0 Ga plutonism and deformation in the SE Amazonian craton: The Archaean granitoids of Marajoara (Carajas Mineral Province, Brazil). Precambrian Research 104, 187–206. https://doi.org/10.1016/S0301-9268(00)00103-0

Amelin, Y.V., Heaman, L.M., Semenov, V.S., 1995. UPb geochronology of layered mafic intrusions in the eastern Baltic Shield: implications for the timing and duration of Paleoproterozoic continental rifting. Precambrian Research 75, 31–46. https://doi.org/10.1016/0301-9268(95)00015-W

Andersen, T., 2005. Detrital zircons as tracers of sedimentary provenance: limiting conditions from statistics and numerical simulation. Chemical Geology 216, 249–270. https://doi.org/10.1016/j.chemgeo.2004.11.013

Antonio, P.Y.J., D'Agrella-Filho, M.S., Trindade, R.I.F., Nédélec, A., de Oliveira, D.C., da Silva, F.F., Roverato, M., Lana, C., 2017. Turmoil before the boring billion: Paleomagnetism of the 1880–1860 Ma Uatumã event in the Amazonian craton. Gondwana Research 49, 106–129. https://doi.org/10.1016/j.gr.2017.05.006

Araújo Filho, R.C., Nogueira, A.C.R., Araújo, R.N., 2020. New stratigraphic proposal of a

paleoproterozoic siliciclastic succession: Implications for the evolution of the Carajás basin, amazonian craton, Brazil. Journal of South American Earth Sciences 102665. https://doi.org/10.1016/j.jsames.2020.102665

Araujo, R., Nogueira, A., 2019. Serra sul diamictite of the carajas basin (Brazil): A paleoproterozoic glaciation on the amazonian craton. Geology 47, 1166–1170. https://doi.org/10.1130/G46923.1

Archer, J.B., 1984. Clastic Intrusions in Deep-Sea Fan Deposits of the Rosroe Formation, Lower Ordovician, Western Ireland. Journal of Sedimentary Petrology 54, 1197–1205. https://doi.org/10.1306/212f8599-2b24-11d7-8648000102c1865d

Arnaud, E., Etienne, J.L., 2011. Recognition of glacial influence in Neoproterozoic sedimentary successions. Geological Society, London 36, 39–50. https://doi.org/10.1144/M36.3

Atkins, C.B., 2004. Photographic atlas of striations from selected glacial and non-glacial environments. Antarctic Data Series 28.

Bindeman, I.N., Zakharov, D.O., Palandri, J., Greber, N.D., Dauphas, N., Retallack, G.J., Hofmann, A., Lackey, J.S., Bekker, A., 2018. Rapid emergence of subaerial landmasses and onset of a modern hydrologic cycle 2.5 billion years ago. Nature 557, 545–548. https://doi.org/10.1038/s41586-018-0131-1

Blake, T.S., 1993. Late Archaean crustal extension, sedimentary basin formation, flood basalt volcanism and continental rifting: the Nullagine and Mount Jope Supersequences, Western Australia. Precambrian Research 60, 185–241. https://doi.org/10.1016/0301-9268(93)90050-C

Cabral, A.R., Bühn, B., Seabra Gomes, A.A., Galbiatti, H.F., Lehmann, B., Halder, S., 2017. Multiple sulfur isotopes from the Neoarchaean Serra Sul black shale, Carajás mineral province, northern Brazil. Journal of South American Earth Sciences 79, 377–383.

https://doi.org/10.1016/j.jsames.2017.08.002

Cabral, A.R., Creaser, R.A., Nägler, T., Lehmann, B., Voegelin, A.R., Belyatsky, B., Pašava, J., Seabra Gomes, A.A., Galbiatti, H., Böttcher, M.E., Escher, P., 2013. Trace-element and multi-isotope geochemistry of Late-Archean black shales in the Carajás iron-ore district, Brazil. Chemical Geology 362, 91–104. https://doi.org/10.1016/j.chemgeo.2013.08.041

Campbell, I.H., Allen, C.M., 2008. Formation of supercontinents linked to increases in atmospheric oxygen. Nature Geoscience 1, 554–558. https://doi.org/10.1038/ngeo259

Caquineau, T., Paquette, J.-L., Philippot, P., 2018. U-Pb detrital zircon geochronology of the Turee Creek Group, Hamersley Basin, Western Australia: Timing and correlation of the Paleoproterozoic glaciations. Precambrian Research 307, 34–50. https://doi.org/10.1016/j.precamres.2018.01.003

Cawood, P.A., Hawkesworth, C.J., Dhuime, B., 2012. Detrital zircon record and tectonic setting. Geology 40, 875–878. https://doi.org/10.1130/G32945.1

Chowdhury, P., Gerya, T., Chakraborty, S., 2017. Emergence of silicic continents as the lower crust peels off on a hot plate-tectonic Earth. Nature Geoscience 10, 698–703. https://doi.org/10.1038/ngeo3010

Claire, M.W., Catling, D.C., Zahnle, K.J., 2006. Biogeochemical modelling of the rise in atmospheric oxygen. Geobiology 4, 239–269. https://doi.org/10.1111/j.1472-4669.2006.00084.x

Cohen, K., Finney, S., Gibbard, P., Fan, J., 2013. The ICS International Chronostratigraphic Chart. Episodes 36, 199–204.

Collinson, J., 1994. Sedimentary deformational structures, in: Maltman, A. (Ed.), The Geological Deformation of Sediments. Springer Science, pp. 95–125. https://doi.org/10.1007/978-94-011-0731-0

Condie, K.C., Kröner, A., 2013. The building blocks of continental crust: Evidence for a major change in the tectonic setting of continental growth at the end of the Archean. Gondwana Research. https://doi.org/10.1016/j.gr.2011.09.011

Cordani, U.G., Ramos, V.A., Fraga, L.M., Cegarra, M., Delgado, I., de Souza, K.G., Gomes, F.E.M., Schobbenhaus, C., 2016. Tectonic map of South America at 1:5.9M. Scale 1: 5 900 000 CGMW-CPRM-.

Corfu, F., Hanchar, J.M., Hoskin, P.W.O., Kinny, P., 2003. Atlas of Zircon Textures, in: Hanchar, J.M., Hoskin, P.W.O. (Eds.), Zircon. Mineralogical Society of America and Geochemical Society, Washington, DC, United States, pp. 469–500.

Coutts, D.S., Matthews, W.A., Hubbard, S.M., 2019. Assessment of widely used methods to derive depositional ages from detrital zircon populations. Geoscience Frontiers 10, 1421–1435. https://doi.org/10.1016/j.gsf.2018.11.002

Dall'Agnol, R., Teixeira, N.P., Rämö, O.T., Moura, C.A.V., Macambira, M.J.B., de Oliveira, D.C., 2005. Petrogenesis of the Paleoproterozoic rapakivi A-type granites of the Archean Carajás metallogenic province, Brazil. Lithos 80, 101–129. https://doi.org/10.1016/j.lithos.2004.03.058

Dalstra, H., Guedes, S., 2004. Giant hydrothermal hematite deposits with Mg-Fe metasomatism: A comparison of the Carajás, Hamersley, and other iron ores. Economic Geology 99, 1793–1800. https://doi.org/10.2113/gsecongeo.99.8.1793

Dardenne, M.A., Ferreira Filho, C.F., Meirelles, M.R., 1988. The role of shoshonitic and calc-alkaline suites in the tectonic evolution of the Carajás District, Brazil. Journal of South American Earth Sciences 1, 363–372. https://doi.org/10.1016/0895-9811(88)90023-5

de Almeida, F.F.M., Brito Neves, B.B., Carneiro, C.D.R., 2000. The origin and evolution of the South American Platform. Earth-Science Reviews 50, 77–111.

https://doi.org/10.1016/S0012-8252(99)00072-0

Dhuime, B., Wuestefeld, A., Hawkesworth, C.J., 2015. Emergence of modern continental crust about 3 billion years ago. Nature Geoscience 8, 552–555. https://doi.org/10.1038/ngeo2466

Dickinson, W.R., Gehrels, G.E., 2009. Use of U–Pb ages of detrital zircons to infer maximum depositional ages of strata: A test against a Colorado Plateau Mesozoic database. Earth and Planetary Science Letters 288, 115–125. https://doi.org/10.1016/j.epsl.2009.09.013

Dreher, A.M., Xavier, R.P., Martini, S.L., 2005. Fragmental rocks if the Igarape Bahia Cu-Au deposits, Carajas minaral Province, Brazil. Revista Brasileira de Geociências 35, 359–368.

Dreher, A.M., Xavier, R.P., Taylor, B.E., Martini, S.L., 2008. New geologic, fluid inclusion and stable isotope studies on the controversial Igarapé Bahia Cu-Au deposit, Carajás Province, Brazil. Mineralium Deposita 43, 161–184. https://doi.org/10.1007/s00126-007-0150-6

Dubois, M., Lopez, M., Orberger, B., Gay, A., Moussavou, M., Pambo, F., Rodrigues, S., 2017. The 2.1 Ga-old injectite network of the Franceville Basin, Gabon: Architecture, origin and implications on manganese mineralization. Precambrian Research 302, 255–278. https://doi.org/10.1016/j.precamres.2017.09.022

Ducassou, C., Mercuzot, M., Bourquin, S., Rossignol, C., Pellenard, P., Beccaletto, L., Poujol, M., Hallot, E., Pierson-Wickmann, A.C., Hue, C., Ravier, E., 2019. Sedimentology and U-Pb dating of Carboniferous to Permian continental series of the northern Massif Central (France): Local palaeogeographic evolution and larger scale correlations. Palaeogeography, Palaeoclimatology, Palaeoecology 533, 109228. https://doi.org/10.1016/j.palaeo.2019.06.001

Eriksson, P.G., Catuneanu, O., Sarkar, S., Tirsgaard, H., 2005. Patterns of sedimentation in the Precambrian. Sedimentary Geology 176, 17–42.

https://doi.org/10.1016/j.sedgeo.2005.01.003

Eriksson, P.G., Condie, K.C., 2014. Cratonic sedimentation regimes in the ca. 2450-2000Ma period: Relationship to a possible widespread magmatic slowdown on Earth? Gondwana Research 25, 30–47. https://doi.org/10.1016/j.gr.2012.08.005

Ernst, R., Bleeker, W., 2010. Large igneous provinces (LIPs), giant dyke swarms, and mantle plumes: Significance for breakup events within Canada and adjacent regions from 2.5 Ga to the present. Canadian Journal of Earth Sciences 47, 695–739. https://doi.org/10.1139/E10-025

Eyles, C.H., Eyles, N., 2000. Subaqueous mass flow origin for Lower Permian diamictites and associated facies of the Grant Group, Barbwire Terrace, Canning Basin, Western Australia. Sedimentology 47, 343–356. https://doi.org/10.1046/j.1365-3091.2000.00295.x

Eyles, N., Januszczak, N., 2004. “Zipper-rift”: A tectonic model for Neoproterozoic glaciations during the breakup of Rodinia after 750 Ma. Earth-Science Reviews 65, 1–73. https://doi.org/10.1016/S0012-8252(03)00080-1

Feio, G.R.L., Dall’Agnol, R., Dantas, E.L., Macambira, M.J.B., Gomes, A.C.B., Sardinha, A.S., Oliveira, D.C., Santos, R.D., Santos, P.A., 2012. Geochemistry, geochronology, and origin of the Neoarchean Planalto Granite suite, Carajás, Amazonian craton: A-type or hydrated charnockitic granites? Lithos 151, 57–73. https://doi.org/10.1016/j.lithos.2012.02.020

Feio, G.R.L., Dall’Agnol, R., Dantas, E.L., Macambira, M.J.B., Santos, J.O.S., Althoff, F.J., Soares, J.E.B., 2013. Archean granitoid magmatism in the Canaã dos Carajás area: Implications for crustal evolution of the Carajás province, Amazonian craton, Brazil. Precambrian Research 227, 157–185. https://doi.org/10.1016/j.precamres.2012.04.007

Flament, N., Coltice, N., Rey, P.F., 2008. A case for late-Archaean continental emergence from

thermal evolution models and hypsometry. Earth and Planetary Science Letters 275, 326–336. https://doi.org/10.1016/j.epsl.2008.08.029

Galarza, M.A., Macambira, M.J.B., Villas, R.N., 2008. Dating and isotopic characteristics (Pb and S) of the Fe oxide-Cu-Au-U-REE Igarapé Bahia ore deposit, Carajás mineral province, Pará state, Brazil. Journal of South American Earth Sciences 25, 377–397. https://doi.org/10.1016/j.jsames.2007.07.006

Gawthorpe, R.L., Leeder, M.R., 2000. Tectono-sedimentary evolution of active extensional basins. Basin Research 12, 195–218. https://doi.org/10.1111/j.1365-2117.2000.00121.x

Gibbs, A.K., Wirth, K.R., Hirata, W.K., Olszewski Jr, W.J., 1986. Age and composition of the Grão Pará groups volcanics, Serra dos Carajás. Revista Brasileira de Geociências 16, 201–211.

Grainger, C.J., Groves, D.I., Tallarico, F.H.B., Fletcher, I.R., 2008. Metallogenesis of the Carajás Mineral Province, Southern Amazon Craton, Brazil: Varying styles of Archean through Paleoproterozoic to Neoproterozoic base- and precious-metal mineralisation. Ore Geology Reviews 33, 451–489. https://doi.org/10.1016/j.oregeorev.2006.10.010

Gumsley, A.P., Chamberlain, K.R., Bleeker, W., Soderlund, U., De Kock, M.O., Larsson, E.R., 2017. Timing and tempo of the Great Oxidation Event. Proceedings of the National Academy of Sciences 114, 1811–1816. https://doi.org/10.1073/pnas.1608824114

Hagadorn, J.W., Bottjer, D.J., 1997. Wrinkle structures: Microbially mediated sedimentary structures common in subtidal siliciclastic settings at the Proterozoic-Phanerozoic transition. Geology 25, 1047–1050. https://doi.org/10.1130/0091-7613(1997)025<1047:WSMMSS>2.3.CO;2

Hietpas, J., Samson, S., Moecher, D., Chakraborty, S., 2011. Enhancing tectonic and provenance information from detrital zircon studies: assessing terrane-scale sampling and grain-scale characterization. Journal of the Geological Society 168, 309–318.

https://doi.org/10.1144/0016-76492009-163

Hodel, F., Trindade, R.I.F., Macouin, M., Meira, V.T., Dantas, E.L., Paixão, M.A.P., Rospabé, M., Castro, M.P., Queiroga, G.N., Alkmim, A.R., Lana, C.C., 2019. A Neoproterozoic hyper-extended margin associated with Rodinia's demise and Gondwana's build-up: The Araguaia Belt, central Brazil. Gondwana Research 66, 43–62. https://doi.org/10.1016/j.gr.2018.08.010

Jackson, S.E., Pearson, N.J., Griffin, W.L., Belousova, E.A., 2004. The application of laser ablation-inductively coupled plasma-mass spectrometry to in situ U–Pb zircon geochronology. Chemical Geology 211, 47–69. https://doi.org/10.1016/j.chemgeo.2004.06.017

Kelly, N.M., Harley, S.L., 2005. An integrated microtextural and chemical approach to zircon geochronology: refining the Archaean history of the Napier Complex, east Antarctica. Contributions to Mineralogy and Petrology 149, 57–84. https://doi.org/10.1007/s00410-004-0635-6

Kim, S.B., Chough, S.K., Chun, S.S., 1995. Bouldery deposits in the lowermost part of the Cretaceous Kyokpori Formation, SW Korea: cohesionless debris flows and debris falls on a steep-gradient delta slope. Sedimentary Geology 98, 97–119. https://doi.org/10.1016/0037-0738(95)00029-8

Klein, C., Ladeira, E.A., 2002. Petrography and Geochemistry of the Least Altered Banded Iron-Formation of the Archean Carajas Formation, Northern Brazil. Economic Geology 97, 643–651. https://doi.org/10.2113/97.3.643

Košler, J., Sláma, J., Belousova, E., Corfu, F., Gehrels, G.E., Gerdes, A., Horstwood, M.S.A., Sircombe, K.N., Sylvester, P.J., Tiepolo, M., Whitehouse, M.J., Woodhead, J.D., 2013. U-Pb detrital zircon analysis - results of an inter-laboratory comparison. Geostandards and

Geoanalytical Research 37, 243–259. https://doi.org/10.1111/j.1751-908X.2013.00245.x

Kump, L.R., Barley, M.E., 2007. Increased subaerial volcanism and the rise of atmospheric oxygen 2.5 billion years ago. Nature 448, 1033–1036. https://doi.org/10.1038/nature06058

Lawrence, R.L., Cox, R., Mapes, R.W., Coleman, D.S., 2011. Hydrodynamic fractionation of zircon age populations. Geological Society of America Bulletin 123, 295–305. https://doi.org/10.1130/B30151.1

Lenhardt, N., Hornung, J., Hinderer, M., Böhnel, H., Torres-Alvarado, I.S., Trauth, N., 2011. Build-up and depositional dynamics of an arc front volcaniclastic complex: The Miocene Tepoztlán Formation (Transmexican Volcanic Belt, Central Mexico). Sedimentology 58, 785–823. https://doi.org/10.1111/j.1365-3091.2010.01203.x

Lowe, D.R., 1982. Sediment gravity flows: II Depositional models with special reference to the deposits of high-density turbidity currents. Journal of Sedimentary Research 52, 279–297.

Ludwig, K.R., 2012. User's Manual for a geochronological toolkit for Microsoft Excel. Berkeley Geochronological Center 75.

Ludwig, K.R., 1998. On the Treatment of Concordant Uranium-Lead Ages. Geochimica et Cosmochimica Acta 62, 665–676. https://doi.org/10.1016/S0016-7037(98)00059-3

Lyons, T.W., Reinhard, C.T., Planavsky, N.J., 2014. The rise of oxygen in Earth's early ocean and atmosphere. Nature 506, 307–315. https://doi.org/10.1038/nature13068

Macambira, M.J.B., Lancelot, J.R., 1996. Time constraints for the formation of the Archean Rio Maria crust, southeastern Amazonian Craton, Brazil. International Geology Review 38, 1134–1142. https://doi.org/10.1080/00206819709465386

Macambira, M.J.B., Vasquez, M.L., Silva, D.C.C., Galarza, M.A., Barros, C.E.M., Camelo, J.F.,

2009. Crustal growth of the central-eastern Paleoproterozoic domain, SW Amazonian craton: Juvenile accretion vs. reworking. Journal of South American Earth Sciences 27, 235–246. https://doi.org/10.1016/j.jsames.2009.02.001

Machado, N., Lindenmayer, Z., Krogh, T.E., Lindenmayer, D., 1991. U-Pb geochronology of Archean magmatism and basement reactivation in the Carajás area, Amazon shield, Brazil. Precambrian Research 49, 329–354. https://doi.org/10.1016/0301-9268(91)90040-H

Malusà, M.G., Carter, A., Limoncelli, M., Villa, I.M., Garzanti, E., 2013. Bias in detrital zircon geochronology and thermochronometry. Chemical Geology 359, 90–107. https://doi.org/10.1016/j.chemgeo.2013.09.016

Marschik, R., Mathur, R., Ruiz, J., Leveille, R.A., de Almeida, A.J., 2005. Late Archean Cu-Au-Mo mineralization at Gameleira and Serra Verde, Carajàs Mineral Province, Brazil: Constraints from Re-Os molybdenite ages. Mineralium Deposita 39, 983–991. https://doi.org/10.1007/s00126-004-0450-z

Martins, P.L.G., Toledo, C.L.B., Silva, A.M., Chemale, F., Santos, J.O.S., Assis, L.M., 2017. Neoarchean magmatism in the southeastern Amazonian Craton, Brazil: Petrography, geochemistry and tectonic significance of basalts from the Carajás Basin. Precambrian Research 302, 340–357. https://doi.org/10.1016/j.precamres.2017.10.013

Martinsen, O., 1994. Mass movements, in: Maltman, A. (Ed.), The Geological Deformation of Sediments. Springer Science, pp. 129–165. https://doi.org/10.1007/978-94-011-0731-0

Melo, G.H.C., Monteiro, L.V.S., Moreto, C.P.N., Xavier, R.P., Silva, M.A.D., 2014. Paragenesis and evolution of the hydrothermal Bacuri iron oxide-copper-gold deposit, Carajás Province (PA). Brazilian Journal of Geology 44, 73–90. https://doi.org/10.5327/Z2317-4889201400010007

Melo, G.H.C., Monteiro, L.V.S., Xavier, R.P., Moreto, C.P.N., Arquaz, R.M., Silva, M.A.D., 2019. Evolution of the Igarapé Bahia Cu-Au deposit, Carajás Province (Brazil): Early syngenetic chalcopyrite overprinted by IOCG mineralization. Ore Geology Reviews 111, 102993. https://doi.org/10.1016/j.oregeorev.2019.102993

Melo, G.H.C., Monteiro, L.V.S., Xavier, R.P., Moreto, C.P.N., Santiago, E.S.B., Dufrane, S.A., Aires, B., Santos, A.F.F., 2017. Temporal evolution of the giant Salobo IOCG deposit, Carajás Province (Brazil): constraints from paragenesis of hydrothermal alteration and U-Pb geochronology. Mineralium Deposita 52, 709–732. https://doi.org/10.1007/s00126-016-0693-5

Moreto, C.P.N., Monteiro, L.V.S., Xavier, R.P., Creaser, R.A., DuFrane, S.A., Tassinari, C.C.G., Sato, K., Kemp, A.I.S., Amaral, W.S., 2015. Neoarchean and paleoproterozoic iron oxide-copper-gold events at the sossego deposit, Carajás Province, Brazil: Re-Os and U-Pb geochronological evidence. Economic Geology 110, 809–835. https://doi.org/10.2113/econgeo.110.3.809

Mougeot, R., 1996. Etude de la limite Archeen-Proterozoique et des minéralisations Au, U associées: Exemples des régions de Jacobina (Etat de Bahia, Brésil) et de Carajas (Etat de Para, Brésil). Université de Montpellier, unpublished.

Mulder, T., Alexander, J., 2001. The physical character of subaqueous sedimentary density flows and their deposits. Sedimentology 48, 269–299.

Myrow, P.M., Tice, L., Archuleta, B., Clark, B., Taylor, J.F., Ripperdan, R.L., 2004. Flat-pebble conglomerate: Its multiple origins and relationship to metre-scale depositional cycles. Sedimentology 51, 973–996. https://doi.org/10.1111/j.1365-3091.2004.00657.x

Nemchin, A.A., Cawood, P.A., 2005. Discordance of the U–Pb system in detrital zircons: Implication for provenance studies of sedimentary rocks. Sedimentary Geology 182, 143–

162. https://doi.org/10.1016/j.sedgeo.2005.07.011

Nemec, W., Steel, R.J., 1984. Alluvial and coastal conglomerates: their significant features and some comments on gravelly mass-flow deposits. Canadian Society of Petroleum Geologists Memoir 10, 1–31. https://doi.org/-

Olsson, J.R., Söderlund, U., Klausen, M.B., Ernst, R.E., 2010. U-Pb baddeleyite ages linking major Archean dyke swarms to volcanic-rift forming events in the Kaapvaal craton (South Africa), and a precise age for the Bushveld Complex. Precambrian Research 183, 490–500. https://doi.org/10.1016/j.precamres.2010.07.009

Olszewski, W.J., Wirth, K.R., Gibbs, A.K., Gaudette, H.E., 1989. The age, origin, and tectonics of the Grão Pará Group and associated rocks, Serra dos Carajás, Brazil: Archean continental volcanism and rifting. Precambrian Research 42, 229–254. https://doi.org/10.1016/0301-9268(89)90013-2

Pesonen, L.J., Elming, S.A., Mertanen, S., Pisarevsky, S., D'Agrella-Filho, M.S., Meert, J.G., Schmidt, P.W., Abrahamsen, N., Bylund, G., 2003. Palaeomagnetic configuration of continents during the Proterozoic. Tectonophysics 375, 289–324. https://doi.org/10.1016/S0040-1951(03)00343-3

Peters, T.J., Valarelli, J.V., Coutinho, J.M.V., Sommerauer, J., von Raumer, J., 1977. The manganese deposits of Buritirama (Pará , Brazil). Schweizerische mineralogische und petrographische Mitteilungen - Bulletin suisse de minéralogie et pétrographie 57, 313–327. https://doi.org/http://dx.doi.org/10.5169/seals-44438 Nutzungsbedingungen

Philippot, P., Ávila, J.N., Killingsworth, B.A., Tessalina, S., Baton, F., Caquineau, T., Muller, E., Pecoits, E., Cartigny, P., Lalonde, S.V., Ireland, T.R., Thomazo, C., Van Kranendonk, M.J., Busigny, V., 2018. Globally asynchronous sulphur isotope signals require re-definition of the Great Oxidation Event. Nature Communications 9, 1–10.

https://doi.org/10.1038/s41467-018-04621-x

Pidgeon, R.T., MacAmbira, M.J.B., Lafon, J.M., 2000. Th-U-Pb isotopic systems and internal structures of complex zircons from an enderbite from the Pium Complex, Carajas Province, Brazil: Evidence for the ages of granulite facies metamorphism and the protolith of the enderbite. Chemical Geology 166, 159–171. https://doi.org/10.1016/S0009-2541(99)00190-4

Pinheiro, R.V.L., Holdsworth, R.E., 1997. Reactivation of Archaean strike-slip fault systems, Amazon region, Brazil. Journal of the Geological Society 154, 99–103. https://doi.org/10.1144/gsjgs.154.1.0099

Pollard, P.J., Taylor, R.G., Peters, L., Matos, F., Freitas, C., Saboia, L., Huhn, S., 2019. 40Ar- 39Ar dating of Archean iron oxide Cu-Au and Paleoproterozoic granite-related Cu-Au deposits in the Carajás Mineral Province, Brazil: implications for genetic models. Mineralium Deposita 54, 329–346. https://doi.org/10.1007/s00126-018-0809-1

Postma, G., 1990. Depositional architecture and facies of river and fan deltas: a synthesis, in: Collela, A., David, B.P. (Eds.), Coarse-Grained Deltas. International Association of Sedimentology Special Publication, pp. 13–28.

Postma, G., Cartigny, M.J.B., 2014. Supercritical and subcritical turbidity currents and their deposits - A synthesis. Geology 42, 987–990. https://doi.org/10.1130/G35957.1

Postma, G., Kleverlaan, K., Cartigny, M.J.B., 2014. Recognition of cyclic steps in sandy and gravelly turbidite sequences, and consequences for the Bouma facies model. Sedimentology 61, 2268–2290. https://doi.org/10.1111/sed.12135

Rasmussen, B., Bekker, A., Fletcher, I.R., 2013. Correlation of Paleoproterozoic glaciations based on U-Pb zircon ages for tuff beds in the Transvaal and Huronian Supergroups. Earth and Planetary Science Letters 382, 173–180. https://doi.org/10.1016/j.epsl.2013.08.037

Ravier, E., Guiraud, M., Guillien, A., Vennin, E., Buoncristiani, J.-F., Portier, E., 2015. Micro- to macro-scale internal structures, diagenesis and petrophysical evolution of injectite networks in the Vocontian Basin (France): Implications for fluid flow. Marine and Petroleum Geology 64, 125–151. https://doi.org/10.1016/j.marpetgeo.2015.02.040

Reddy, S.M., Evans, D.A.D., 2009. Palaeoproterozoic supercontinents and global evolution: Correlations from core to atmosphere. Geological Society Special Publication 323, 1–26. https://doi.org/10.1144/SP323.1

Requia, K., Stein, H., Fontboté, L., Chiaradia, M., 2003. Re-Os and Pb-Pb geochronology of the Archean Salobo iron oxide copper-gold deposit, Carajás mineral province, northern Brazil. Mineralium Deposita 38, 727–738. https://doi.org/10.1007/s00126-003-0364-1

Ribeiro da Luz, B., Crowley, J.K., 2012. Morphological and chemical evidence of stromatolitic deposits in the 2.75Ga Carajás banded iron formation, Brazil. Earth and Planetary Science Letters 355–356, 60–72. https://doi.org/10.1016/j.epsl.2012.08.028

Rohais, S., Eschard, R., Guillocheau, F., 2008. Depositional model and stratigraphic architecture of rift climax Gilbert-type fan deltas (Gulf of Corinth, Greece). Sedimentary Geology 210, 132–145. https://doi.org/10.1016/j.sedgeo.2008.08.001

Ronze, P.C., Soares, A.D.V., Santos, M.G.S., Barreira, C.F., 2000. Alemao copper-gold (U-REE) deposits, Carajas, Brazil, in: Porter, T.M. (Ed.), Hydrothermal Iron Oxide Copper-Gold and Related Deposits: A Global Perspective. PCG Publishing, pp. 191–202.

Rossignol, C., Bourquin, S., Poujol, M., Hallot, E., Dabard, M.-P., Nalpas, T., 2016. The volcaniclastic series from the Luang Prabang Basin, Laos: A witness of a triassic magmatic arc? Journal of Asian Earth Sciences 120. https://doi.org/10.1016/j.jseaes.2016.02.001

Rossignol, C., Hallot, E., Bourquin, S., Poujol, M., Jolivet, M., Pellenard, P., Ducassou, C., Nalpas, T., Heilbronn, G., Yu, J., Dabard, M.-P., 2019. Using volcaniclastic rocks to constrain

sedimentation ages: To what extent are volcanism and sedimentation synchronous? Sedimentary Geology 381, 46–64. https://doi.org/10.1016/J.SEDGEO.2018.12.010

Roverato, M., 2016. The Montesbelos mass-flow (southern Amazonian craton, Brazil): a Paleoproterozoic volcanic debris avalanche deposit? Bulletin of Volcanology 78. https://doi.org/10.1007/s00445-016-1043-2

Roverato, M., Juliani, C., Dias-Fernandes, C.M., Capra, L., 2017. Paleoproterozoic andesitic volcanism in the southern Amazonian craton, the Sobreiro Formation: New insights from lithofacies analysis of the volcaniclastic sequences. Precambrian Research 289, 18–30. https://doi.org/10.1016/j.precamres.2016.11.005

Rubatto, D., 2002. Zircon trace element geochemistry: partitioning with garnet and the link between U–Pb ages and metamorphism. Chemical Geology 184, 123–138. https://doi.org/10.1016/S0009-2541(01)00355-2

Rubi, R., Rohais, S., Bourquin, S., Moretti, I., Desaubliaux, G., 2018. Processes and typology in Gilbert-type delta bottomset deposits based on outcrop examples in the Corinth Rift. Marine and Petroleum Geology 92, 193–212. https://doi.org/10.1016/j.marpetgeo.2018.02.014

Salminen, J., Oliveira, E.P., Piispa, E.J., Smirnov, A.V., Trindade, R.I.F., 2019. Revisiting the paleomagnetism of the Neoarchean Uauá mafic dyke swarm, Brazil: Implications for Archean supercratons. Precambrian Research 329, 108–123. https://doi.org/10.1016/j.precamres.2018.12.001

Santos, J.O.S., Hartmann, L.A., Gaudette, H.E., Groves, D.I., Mcnaughton, N.J., Fletcher, I.R., 2000. A New Understanding of the Provinces of the Amazon Craton Based on Integration of Field Mapping and U-Pb and Sm-Nd Geochronology. Gondwana Research 3, 453–488. https://doi.org/10.1016/S1342-937X(05)70755-3

Santos, M.M., Lana, C., Scholz, R., Buick, I., Schmitz, M.D., Kamo, S.L., Gerdes, A., Corfu, F., Tapster, S., Lancaster, P., Storey, C.D., Basei, M.A.S., Tohver, E., Alkmim, A.R., Nalini, H., Krambrock, K., Fantini, C., Wiedenbeck, M., 2017. A New Appraisal of Sri Lankan BB Zircon as a Reference Material for LA-ICP-MS U-Pb Geochronology and Lu-Hf Isotope Tracing. Geostandards and Geoanalytical Research 41, 335–358. https://doi.org/10.1111/ggr.12167

Sardinha, A.S., Barros, C.E.M., Krymsky, R., 2006. Geology, geochemistry, and U-Pb geochronology of the Archean (2.74 Ga) Serra do Rabo granite stocks, Carajás Metallogenetic Province, northern Brazil. Journal of South American Earth Sciences 20, 327–339. https://doi.org/10.1016/j.jsames.2005.11.001

Sharman, G.R., Malkowski, M.A., 2020. Needles in a haystack: Detrital zircon U Pb ages and the maximum depositional age of modern global sediment. Earth-Science Reviews 103109. https://doi.org/10.1016/j.earscirev.2020.103109

Shore, M., Fowler, A.D., 1996. Oscillatory zoning in minerals: a common phenomenon. The Canadian Mineralogist 34, 1111–1126.

Siepierski, L., Ferreira Filho, C.F., 2016. Spinifex-textured komatiites in the south border of the Carajas ridge, Selva Greenstone belt, Carajás Province, Brazil. Journal of South American Earth Sciences 66, 41–55. https://doi.org/10.1016/j.jsames.2015.12.011

Silva, F.F.D., Oliveira, D.C.D., Antonio, P.Y.J., D'Agrella-Filho, M.S., Lamarao, C.N., 2016. Bimodal magmatism of the Tucumã area, Carajás province: U-Pb geochronology, classification and processes. Journal of South American Earth Sciences 72, 95–114. https://doi.org/10.1016/j.jsames.2016.07.016

Sircombe, K.N., Stern, R.A., 2002. An investigation of artificial biasing in detrital zircon U-Pb geochronology due to magnetic separation in sample preparation. Geochimica et

Cosmochimica Acta 66, 2379–2397.

Sláma, J., Košler, J., 2012. Effects of sampling and mineral separation on accuracy of detrital zircon studies. Geochemistry Geophysics Geosystems 13, Q05007. https://doi.org/10.1029/2012GC004106

Sláma, J., Košler, J., Condon, D.J., Crowley, J.L., Gerdes, A., Hanchar, J.M., Horstwood, M.S.A., Morris, G.A., Nasdala, L., Norberg, N., Schaltegger, U., Schoene, B., Tubrett, M.N., Whitehouse, M.J., 2008. Plešovice zircon — A new natural reference material for U–Pb and Hf isotopic microanalysis. Chemical Geology 249, 1–35. https://doi.org/10.1016/j.chemgeo.2007.11.005

Steiger, R.H., Jäger, E., 1977. Subcommission on geochronology: convention on the use of decay constants in geo- and comsochronology. Earth and Planetary Science Letters 36, 359–362.

Tallarico, F.H.B., Figueiredo, B.R., Groves, D.I., Kositcin, N., McNaughton, N.J., Fletcher, I.R., Rego, J.L., 2005. Geology and SHRIMP U-Pb geochronology of the Igarapé Bahia deposit, Carajás copper-gold belt, Brazil: An Archean (2.57 Ga) example of Iron-Oxide Cu-Au-(U-REE) mineralization. Economic Geology 100, 7–28. https://doi.org/10.2113/100.1.0007

Tassinari, C.C.G., Mellito, K.M., Babinski, M., 2003. Age and origin of the Cu (Au-Mo-Ag) Salobo 3A ore deposit, Carajas Mineral Province, Amazonian Craton, northern Brazil. Episodes 26, 2–9.

Tavares, F.M., Trouw, R.A.J., da Silva, C.M.G., Justo, A.P., Oliveira, J.K.M., 2018. The multistage tectonic evolution of the northeastern Carajás Province, Amazonian Craton, Brazil: Revealing complex structural patterns. Journal of South American Earth Sciences 88, 238–252. https://doi.org/10.1016/j.jsames.2018.08.024

Teipel, U., Eichhorn, R., Loth, G., Rohrmüller, J., Höll, R., Kennedy, A., 2004. U-Pb SHRIMP and

Nd isotopic data from the western Bohemian Massif (Bayerischer Wald, Germany): Implications for Upper Vendian and Lower Ordovician magmatism. International Journal of Earth Sciences 93, 782–801. https://doi.org/10.1007/s00531-004-0419-2

Teitler, Y., Le Hir, G., Fluteau, F., Philippot, P., Donnadieu, Y., 2014. Investigating the Paleoproterozoic glaciations with 3-D climate modeling. Earth and Planetary Science Letters 395, 71–80. https://doi.org/10.1016/j.epsl.2014.03.044

Teixeira, J.B.G., Eggler, D.H., 1994. Petrology, geochemistry, and tectonic setting of Archean basaltic and dioritic rocks from the N4 iron deposit, Serra dos Carajás, Pará, Brazil. Acta Geologica Leopoldensia 17, 71–114.

Teixeira, W., Hamilton, M.A., Girardi, V.A.V., Faleiros, F.M., Ernst, R.E., 2019. U-Pb baddeleyite ages of key dyke swarms in the Amazonian Craton (Carajás/Rio Maria and Rio Apa areas): Tectonic implications for events at 1880, 1110 Ma, 535 Ma and 200 Ma. Precambrian Research 329, 138–155. https://doi.org/10.1016/j.precamres.2018.02.008

Tolbert, G.E., Tremaine, J.W., Melcher, G.C., Gomes, C.B., 1971. The Recently Discovered Serra dos Carajás Iron Deposits, northern Brazil. Economic Geology 66, 985–994. https://doi.org/https://doi.org/10.2113/gsecongeo.66.7.985

Toledo, P.I.F., Moreto, C.P.N., Xavier, R.P., Gao, J.F., de Matos, J.H.S.N., de Melo, G.H.C., 2019. Multistage evolution of the Neoarchean (ca. 2.7 Ga) Igarapé cinzento (GT-46) iron oxide copper-gold deposit, Cinzento shear zone, Carajás Province, Brazil. Economic Geology 114, 1–34. https://doi.org/10.5382/econgeo.2019.4617

Trendall, A.F., Basei, M.A.S., De Laeter, J.R., Nelson, D.R., 1998. SHRIMP zircon U-Pb constraints on the age of the Carajas formation, Grao Para Group, Amazon Craton. Journal of South American Earth Sciences 11, 265–277. https://doi.org/10.1016/S0895-9811(98)00015-7

Vasquez, M.L., Rosa-Costa, L.T., 2008. Geologia e recursos minerais do estado do Pará: texto explicativo. CPRM - Serviço Geologico do Brasil 328.

Vasquez, M.L., Sousa, C.S., Carvalho, J.M.A., 2008. Mapa Geológico do Estado do Pará. Scale 1:1 000 000.

Vennin, E., Olivier, N., Brayard, A., Bour, I., Thomazo, C., Escarguel, G., Fara, E., Bylund, K.G., Jenks, J.F., Stephen, D.A., Hofmann, R., 2015. Microbial deposits in the aftermath of the end-Permian mass extinction: A diverging case from the Mineral Mountains (Utah, USA). Sedimentology 62, 753–792. https://doi.org/10.1111/sed.12166

Vermeesch, P., 2012. On the visualisation of detrital age distributions. Chemical Geology 312–313, 190–194. https://doi.org/10.1016/j.chemgeo.2012.04.021

Walker, R.G., 1975. Generalized facies models for resedimented conglomerates of turbidite association. Bulletin of the Geological Society of America 86, 737–748. https://doi.org/10.1130/0016-7606(1975)86<737:GFMFRC>2.0.CO;2

Williams, G.E., Schmidt, P.W., Young, G.M., 2016. Strong seasonal Proterozoic glacial climate in low paleolatitudes: radically different climate system on the pre-Ediacarian Earth. Geoscience Frontiers 7, 555–571. https://doi.org/10.1016/j.gsf.2016.01.005

Wirth, K.R., Gibbs, A.K., Olszewski, W.J., 1986. U-Pb ages of zircons from the Grão-Pará Group and Serra dos Carajás Granites, Pará, Brazil. Revista Brasileira de Geociências 16, 195–200.

Zimmermann, S., Mark, C., Chew, D., Voice, P.J., 2018. Maximising data and precision from detrital zircon U-Pb analysis by LA-ICPMS: The use of core-rim ages and the single-analysis concordia age. Sedimentary Geology 1–9. https://doi.org/10.1016/J.SEDGEO.2017.12.020

Figures and tables caption

Figures

Figure 1. Location of the Amazonian Craton and the Carajás Basin.

A. Schematic West Gondwana reconstruction of the main tectonic elements of South America and Africa. Modified after (Cordani et al., 2016). A: Amazonian Craton; SF: São Francisco Craton; WA: West African Craton.

B. Location of the Carajás Basin within the Amazonian Craton. Adapted after Almeida et al. (2013); Cordani et al. (2016), de Almeida et al. (2000) and Santos et al. (2000).

Figure 2. Main sedimentary units of the Carajás Basin.

Adapted after Araújo and Nogueira (2019); Klein and Ladeira (2002) and Trendall et al. (1998). This synthetic log applies for the central part of the Carajás Basin. In other parts of the basin, other stratigraphic subdivisions have been proposed (i.e., Rio Novo, São Félix, Aquiri, Pojuca and Salobo and São Sebastião groups, mostly equivalent to the Grão Pará Group, e.g., Vasquez et al., 2008).

Figure 3. Geological map of the Carajás Basin and location of the studied drill-cores.

A. Geological map of the Carajás Basin (after Vasquez et al., 2008).

B. Location of the drill-cores. Fm: Formation. Mapping of the Serra Sul Formation modified after Araújo Filho et al. (2020). Coordinates and complete references of the drill-cores are available in the Appendix 1.

Figure 4. Chronological framework for the main sedimentary units of the Carajás Basin.

Numbers refers to the Table 1. Arrows indicate the range of potential depositional ages for sedimentary units attached to them. Stratigraphic chart: International Chronostratigraphic Chart v2020/01 (Cohen et al., 2013).

Figure 5. Sedimentological logs of the drill-cores intersecting the Serra Sul Formation along with locations of the dated samples.

Facies codes are provided in Table 2. The location of the drill-cores is depicted in the Fig. 3B and given in the Appendix 1.

Figure 6. Reconstruction of the depositional environments of the Serra Sul Formation.

The different facies are described in Table 2, and facies associations (FA) defining each depositional environment are given in Table 4.

Figure 7. Overview photographs of the conglomeratic facies identified in the Serra Sul Formation.

Facies are described in Table 2. Arrows point to the stratigraphic up.

A. Sample GT12 427.10. Polymictic conglomerate showing a normal grading from conglomerate to fine sandstone. Stratigraphic top to the right.

B. Sample FD02 179.10. Clasts supported polymictic conglomerate. The clasts are mainly rounded to sub-rounded and are embedded in a reddish sandy matrix. Some clasts display a high sphericity while other are very elongated.

C. Sample GT12 314.75. Clasts supported polymictic conglomerate with rounded, mostly spherical to sub-spherical clasts embedded in a greenish sandy to silty matrix.

D. Sample GT13 187.50. Polymictic conglomerate with oriented clasts. The clasts display various shapes, most of the whitish cherty clasts are elongated, oriented and sub-angular to sub-rounded in shape, while reddish silty clasts are well-rounded. The matrix is made up of a reddish sandstone.

E. Sample GT13 210.50. Flat pebble conglomerate comprising elongated, sub-angular to sub-rounded clasts embedded within a greenish matrix. Some sandy clasts exhibit original sedimentary structure (top right).

F. Sample GT16 297.55. Flat pebble conglomerate comprising mainly rounded to sub-angular clasts embedded within a greenish matrix.

G. Sample GT16 296.50. Flat pebble conglomerate comprising elongated, plastically deformed angular clasts embedded within a coarse greenish matrix.

Figure 8. Overview photographs of the sandstones and fine-grained facies identified in the Serra Sul Formation.

Facies are described in Table 2. Arrows point to the stratigraphic up.

A. Sample GT12 379.70. Coarse sandstone containing floating clasts, including rounded white sandy clast (center) and small blackish mud clasts (right).

B. Sample GT16 210.10. Massive, medium-grained sandstone with floating clast.

C. Sample GT13 267. Planar lamination underlined by fine sandstone to siltstone layers. The coarser layers (S1 facies) usually contain numerous diagenetic pyrite.

D. Sample GT13 267.40. F1 facies with starved ripples made up of fine sandstone alternating with black siltstone.

E. Sample GT13 215.15. Coarser layer (S1 facies) with slightly erosive base comprising well rounded clasts.

F. Sample FD02 444.80. Millimetric thick crinkled laminations rhythmically organized in centimetric thick sets, interpreted as representing a microbial mat.

G. Sample FD02 401.15. Dark, elongated clot, probably rich in organic matter, embedded in a greyish silty to clayish matrix containing secondary pyrite mineralization.

Figure 9. Overview photographs of the syn- to post-depositional deformations affecting the deposits of the Serra Sul Formation.

Arrows point to the stratigraphic up.

A. Sample GT13 213.15. Slump fold.

B. Sample FD02 381.30. Convoluted lamination.

C. Sample GY 16 211.10 Injectite (clastic dyke and sill) within the fine-grained sediments.

D. Sample FD02 372.60. Load cast occurring at the boundary between coarse grained sandstone and black siltstone.

E. Sample GT13 263.10. Centimetric scale inverse syn-sedimentary fault.

F. Sample GT13 186.05. Folding of heterogeneous material comprising coarse sand, fine sand, gravels and pebbles. White triangles indicate axes of some highly convoluted folds. The differential competence of the heterogeneous material resulted in the buckling of incompetent fine sandstones around competent pebbles. Note that the clast occurring in the

center of this photograph has been erroneously interpreted as a dropstone by Araújo and Nogueira (2019).

Figure 10. Cathodoluminescence images of representative zircon grains of the Serra Sul Formation.

Red circles indicate the location of analyses. Uncertainties are given at the 2σ level.

A. Sample GT16 296.14-296.32

B. Sample GT16 295.85-296.07

C. Sample GT16 279.96-280.09

D. Sample GT16 250.40-250.55

E. Sample GT16 174.29-174.45

F. Sample GT16 140.51-140.65

G. Sample GT16 134.15-134.45

H. Sample GT13 213.85-214.00

I. Sample GT13 211.95-212.15

J. Sample GT13 200.50-200.65

K. Sample GT13 185.95-186.15

L. Sample GT12 353.40-353.70

M. Sample FD02 119.15-118.80

Figure 11. Geochronological diagrams for the Serra Sul Formation.

All the diagrams were generated using Isoplot/Ex 3.00 (Ludwig, 2012). Error ellipses are depicted at the 2σ level.

A. Analyses used to calculate the Maximum Depositional Age (MDA) are depicted in dark blue. Other concordant analyses are depicted by pale blue. The weighted mean error ellipse (concordia date) of the youngest cluster of concordant grains is depicted in pink. Samples collected in the same drill cores are presented according to their stratigraphic position (i.e., samples collected in the bottom of the drill cores to the bottom, samples collected to the top of the drill cores to the top). The number of analyses, the mean square weighted deviate for concordance and equivalence and the probability for concordance and equivalence for each MDA are provided in Table 5.

B. Maximum depositional age calculated from the youngest grains of five samples, assuming the grains are cogenetic in origin. N_a: number of analyses; N_{zrc}: number of zircon grains; MSWD: Mean Square Weighted Deviate for concordance and equivalence; Prob.: probability for concordance and equivalence.

Figure 12. Histograms and age probability distribution diagrams.

The kernel density was estimated using a bandwidth (h) of 14 from the concordant ages of all samples from the Serra Sul Formation using Density Plotter 8.5; (Vermeesch, 2012). N_a: number of analyses, N_{zr}: number of zircon grains.

Figure 13. Chart summarizing the new age constraints along with the main early Paleoproterozoic paleoenvironmental changes and global tectonics events occurring during the late Neoarchean to early Paleoproterozoic.

Main age constraints and significance: see. Fig. 4. The asterisk denotes the newly obtained maximum depositional age for the Serra Sul Formation (Fig. 11B). The arrow indicates the

range of potential depositional ages for the Serra Sul Formation, compare with Fig. 4. Ages for the glacial events are from Rasmussen et al. (2013) and Gumsley et al. (2017). Pilbara Craton after Blake (1993), Kaapvaal Craton after Olsson et al. (2010), São Francisco Craton after Alkmim and Martins-Neto (2012), Karelian-Kola Craton after Amelin et al. (1995), Superior Craton after Ernst and Bleeker (2010), Supervalbara supercontinent after Gumsley et al., (2017) and Salminen et al. (2019). Or.: Orosirian.

Tables

Table 1. Summary of age constraints for the main sedimentary units of the Carajás Basin.

Table 2. Sedimentary facies of the Serra Sul Formation.

Table 3. Petrographic features of representative samples from the Serra Sul Formation.

Table 4. Facies associations of the Serra Sul Formation.

Table 5. Summary of maximum depositional ages from the Serra Sul Formation.

Appendices

Appendix 1. Coordinates of the studied drill cores.

Appendix 2. Analytical methods for U-Pb dating on zircon grains.

Appendix 3. Description of zircon grains typography.

Appendix 4. Analytical results for U-Pb dating on zircon grains from the Serra Sul Formation.

Appendix 5. Complementary geochronological diagrams.

Highlights

- The Serra Sul Formation corresponds to subaqueous depositional environments
- There is no evidence of glacial environments for the Serra Sul diamictite
- The Serra Sul Formation has a maximum depositional age of 2684 ± 10 Ma

Table 1. Summary of age constraints for the main sedimentary units of the Carajás Basin.

Number in Fig. 3	Dating method and interpretation	Reference
Parauapebas Formation		
1	U-Pb dating on zircon grains extracted from a metarhyolite: 2760 ± 11 Ma. Depositional age.	Trendall et al., 1998
2	U-Pb dating on zircon grains extracted from a metarhyolite: 2759 ± 2 Ma. Depositional age.	Machado et al., 1991
3	U-Pb dating on zircon grains extracted from a metabasalt: 2749.6 ± 6.5 Ma. Depositional age.	Martins et al., 2017
Carajás Formation		
4	U-Pb dating on zircon grains extracted from a "probable tuff": 2743 ± 11 Ma. Depositional age.	Trendall et al., 1998
5	U-Pb dating on zircon grains extracted from an intrusive dolerite sill: 2740 ± 8 Ma. Minimum depositional age.	Trendall et al., 1998
Itacaiúnas Supergroup		
6	U-Pb dating zircon grains extracted from a gabbro of the Planalto magmatic suite, intruding the Itacaiúnas Supergroup: 2735 ± 5 Ma. Minimum depositional age.	Feio et al., 2012
Águas Claras Formation		
7	U-Pb dating on detrital zircon grains: 2681 ± 5 Ma. Zircon grains are suggested to derive from coeval volcanic activity: the date is interpreted as a depositional age.	Trendall et al., 1998
8	No Mass Independent Sulfur Fractionation, suggesting a deposition after the beginning of the Great Oxidation Event. Interpreted as a maximum depositional age.	Fabre et al., 2011

9	U-Pb dating zircon grains extracted from the Carajás granite, intruding the Águas Claras Formation: 1880 ± 2 Ma. Minimum depositional age.	Machado et al., 1991

Uncertainties are given at the 2σ level, when relevant.
Note that ages #7 and #8 are mutually inconsistent.

Table 2. Sedimentary facies of the Serra Sul Formation.

Code	Lithology	Sedimentary structures	Depositional processes
Conglomerate			
G1	Polymictic, poorly sorted, matrix- to clast-supported conglomerate. Clasts exhibit angular to rounded shapes and are made up of BIF, mafic volcanic rocks, cherts or black to grey mudstone, quartz, metamorphic rocks. Matrix made up silts to coarse sand (Fig. 7A, 7B, 7C and 7D). Bed thickness: dm to tens of m.	Ungraded, sometimes normally graded (Fig. 7A) with upward increase in matrix. Mud clasts generally exhibit plastic deformation. Generally randomly oriented clasts. (Fig. 7B and 7C) A few beds exhibit clasts fabric (Fig. 7D). Non-erosive or slightly erosive base.	Subaqueous mass flow, cohesive debris flow or hyper-concentrated density flow (Walker, 1975; Lowe, 1982; Nemec and Steel, 1984; Mulder and Alexander, 2001; Postma et al., 2014).
G2	Flat pebbles conglomerate, matrix to clast-supported (Fig. 7E, 7F and 7G). Clasts are elongated and generally exhibit sub-rounded to rounded shapes (a few clasts are sometimes sub-angular). Clasts are intraformational in nature and are made up of sand, silt to clay, or a mixture of sand and silts. The matrix is made up of similar material (fine sand, silt, clay). Bed thickness: dm to m.	Ungraded. The clasts generally exhibit an orientation. Non-erosive to slightly erosive base.	Failure and mass movement of loosely consolidated sediments and/or wave or storm reworking of shoreline deposits (Myrow et al., 2004).
Sandstone			
S1	Medium to very coarse (gravel) sand with floating clasts (Fig. 8A), gravels, sometimes intraformational muddy ripped up clasts. Bed thickness: dm to m.	Massive, inverse to normal or normal grading, sometimes with horizontal planar bedding or trough-cross bedding. Few occurrences of contorted beds.	Hyper-concentrated density flow to turbidity flow (Lowe, 1982; Mulder and Alexander, 2001) or rapid suspension fallout (Postma, 1990).
S2	Various lithologies, mainly sand and silt. Thickness: dm to several meters.	Chaotic horizons, disordered or strongly folded.	Slump and/or slide (Martinsen, 1994)
Fine			
F1	Greyish fine to medium sandstone, silt and clay, with some occurrences thin (cm) coarser (up to coarse sand) beds (Fig. 8C, D). Bed thickness: cm to dm.	Generally laminated (mm to cm thick laminaes), sometimes massive. A few starved ripples occur in the fine to medium sandstone layers. A few oscillatory ripples. Common occurrence of syn-sedimentary faults, water escape and load casts structures.	Deposition from suspension (silt and clay) alternating with tractive current (starved current ripples), sometime reworked by wave current at their top.
F2	Dark grey to black silt to clay (black shale), rich in organic matter. Continuous transition with F1 facies. Bed thickness: cm to dm.	Planar lamination.	Deposition from suspension.
F3	Greyish fine to medium sandstone alternating with silt beds. This facies is associated to the M1 facies. Bed thickness: cm to dm.	Finelly laminated (mm to cm thick laminaes), with occurrence current ripples and symmetrical ripples.	Deposition from suspension with minor tidal and wave ripples.
Other facies			
M1	Fine sandstone alternating with thin (mm) black, organic rich layers (Fig. 8F). Bed thickness: mm to cm.	Millimetric thick crinkled laminations rhythmically organized in centimetric thick sets.	Interpreted as fine sandstone alternating with microbial mats (Hagadorn and Bottjer, 1997).
M2	Dark, organic rich clots with diffuse boundaries embeded in a grey carbonated matrix (Fig. 8G). Bed thickness: dm.	The dark clot masses exhibiting a prefered orientation. Secondary pyrite mineralization.	Tentatively interpreted as reworked microbial mats.

Table 3. Petrographic features of representative samples from the Serra Sul Formation.

Sample	Composition and texture
GT13 – 211.35	Quartz wacke. Small current ripple marks and horizontal lamination underlined by change in grain size. The coarser laminas are made up of small, sub-angular to rounded quartz grains, minute polycrystalline quartz grains and small muscovite flakes. Laminas with finer grain size (silts) mainly comprise minute quartz grains within a blackish matrix.
GT13 – 212.05	Quartz wacke. Sandstone with medium grain-size, coarsely laminated, comprising rounded to angular quartz grains. Muscovite flakes. A few polycrystalline quartz grains and chert fragments. Opaque minerals. Dark silty matrix. Zircon grains.
GT13 – 213.95	Feldspathic wacke. Fine to medium sandstone, with horizontal laminations underlined by a preferential orientation of the grains. Most of the grains are made up of strongly seritized feldspar. A few sub-rounded to sub-angular quartz grains. Opaque minerals. Silty matrix. Secondary chlorite. Zircon grains.
GT13 – 218.25	Quartz wacke. Fine sandstone alternating with blackish siltstone, comprising rounded to sub-angular quartz grains and displaying flame structures. A few small muscovite flakes. Secondary opaque mineral (pyrite).
GT13 – 244.95	Quartz wacke. Very fine sandstone lenses comprising mainly quartz grains, a few muscovite flakes and a few opaque minerals, alternating with black siltstone, sometimes disturbed by millimetric scale syn-sedimentary fault or fluid escape structures. Blackish silty matrix.
GT16 – 102.20	Lithic arenite. Sandstone displaying cross-laminations and comprising mainly lithic fragments. Most of the lithic fragments are rounded to sub-angular and made up of chert and microcrystalline quartz. A few lithic fragments exhibit a microgranular or granular texture, sometimes with quartz grains displaying undulatory extinction. Other lithic fragments are made up of silty material. Weathered feldspars, muscovite, opaque minerals, biotite. A few veins crosscut the sample.
GT16 – 114.95	Quartz wacke. Sandstone displaying wave ripple marks made up of well sorted quartz grains, displaying rounded to elongated shapes. Muscovite flakes. Opaque minerals. Silty, blackish to grey matrix. Very thin veins crosscutting the sample.
GT16 – 130.25	Conglomerate. The conglomerate comprises mainly large angular silty to mud clasts and smaller rounded to sub-rounded clasts of various origins. Most of the clasts are made up of microcrystalline quartz grains, silty material, or with a granular texture (quartz and alkaline feldspar). The matrix of the conglomerate comprises large, mainly rounded monocrystalline quartz sometimes displaying undulatory texture, large feldspar grains, silty material, muscovite flakes, opaque minerals and chlorite.
GT16 – 134.20	Conglomerate. Very poorly sorted conglomerate comprising rounded clasts of various origins (polymictic conglomerate). Some rounded clasts exhibit a microgranular texture, some are made up of microcrystalline quartz (chert), other are made up of metamorphic rock (quartzite) clasts. Some clasts exhibit a granular texture. A few strongly weathered clasts display a microlithic texture. Rounded monocrystalline quartz grains, sometimes displaying undulatory extinction. Chlorite. Muscovite. Opaque minerals (various types, some are very fine grained and disseminated in the matrix, others are comprised within the clasts). Zircon grains.
GT16 – 140.60	Matrix of a conglomerate. Moderately sorted angular to sub-rounded quartz grains, sometimes displaying undulatory extinction. A few lithic fragments, mainly displaying a microgranular texture. Some fragments are made up of chert or silts. A few muscovite flakes. Opaque minerals disseminated within the matrix. Chlorite. Zircon grains. Small veins crosscutting the sample.
GT16 – 260.60	Matrix of a conglomerate. Relatively well sorted sub-angular to sub-rounded quartz grains, sometimes displaying undulatory extinction. Alkaline feldspar displaying various weathering states (from slightly weathered to completely seritized). Lithic fragments of various origins and shapes (from rounded to angular), comprising rounded elements with granular or microgranular texture, chert fragments, silty intraformational rounded clasts. A few muscovite flakes. Opaque minerals disseminated within the matrix. Secondary chlorite. A few veins crosscut the sample.
GT16 – 280.00	Lithic arenite. Coarse, moderately sorted sandstone made up of lithic fragments and monocrystalline quartz grains. The lithic fragments are made up of chert or polycrystalline quartz fragments with a granular texture. A few clasts exhibit a spherulitic texture and are interpreted to be volcanic in origin. Chlorite. Opaque minerals. Biotite. Zircon grains
GT16 – 296.20	Flat pebble conglomerate.

	This conglomerate is made up of rounded, nearly spherical to elongated clasts mainly consisting of very fine sandstone of siltstone. A few clasts are made up polycrystalline quartz grains with a granular texture. The matrix comprises rounded to sub-angular monocrystalline quartz grains embedded within silty material. Chlorite. Zircon grains.

Table 4. Facies associations of the Serra Sul Formation.

Code	Facies association	Depositional environment
FA1	G1, S1, F1, F2	Deep water association (Walker, 1975; Postma and Cartigny, 2014).
FA2	G2, S1, S2, rare occurrence of G1	Shoreface to upper offshore, high-energy environment (Myrow et al., 2004).
FA3	F1, F3, M1, M2, rare occurrence of S2	Shallow water, low-energy environment with development of microbialite (Hagadorn and Bottjer, 1997).

Table 5. Summary of maximum depositional ages from the Serra Sul Formation.

Sample	N_{zr}	Probability of concordance ≥ 10%, decay constants errors included								
		Detection limits (%)				Maximum depositional age				
		$DL_{1(pL=0.5)}$	$DL_{1(pL=0.95)}$	$DL_{3(pL=0.5)}$	$DL_{1(pL=0.95)}$	Concordia age	± (2σ)	n	MSWD	Probability
Drill core: GT16										
GT16 - 134.15-134.45	77	0.9	3.8	3.5	8.0	2815.8	8.8	10	1.4	0.12
GT16 - 140.51-140.65	22	3.1	12.7	12.0	26.0	2748	12	5	0.65	0.75
GT16 - 174.29-174.45	52	1.3	5.6	5.2	11.7	2708	11	10	0.67	0.85
GT16 - 250.40-250.55	22	3.1	12.7	12.0	26.0	2767	14	4	0.94	0.47
GT16 - 279.96-280.09	67	1.0	4.4	4.0	9.1	2718	12	7	0.95	0.50
GT16 - 295.85-296.07	33	2.1	8.7	8.1	17.9	2786	12	5	1.5	0.13
GT16 - 296.14-296.32	75	0.9	3.9	3.6	8.2	2770.1	8.9	10	0.67	0.85
Drill core: GT13										
GT13 - 185.95-186.15	11	6.3	23.8	23.6	47.1	2706	12	8	0.61	0.87
GT13 - 200.50-200.65	2	29.3	77.6	na	na	*2947*	*23*	*2*	*0.34*	*0.80*
GT13 - 211.95-212.15	54	1.3	5.4	5.0	11.3	2701.6	9.2	10	0.40	0.99
GT13 - 213.85-214.00	32	2.1	8.9	8.3	18.4	**2674**	**17**	4	1.5	0.17
Drill core: GT12										
GT12 - 353.40-353.70	12	5.6	22.1	21.7	43.9	2821.3	9.3	9	0.76	0.74
Drill core: FD02										
FD02 - 119.15-118.80	13	5.2	20.6	20.1	41.1	2722.8	8.3	14	0.58	0.96
Pooled results										
All samples	472					2684	10	10	0.62	0.89

N_{zr}: number of concordant zircon grain analyzed per sample; n: number of analyses used to calculate the maximum deposition age; DL_1: detection limit for at least one grain; DL_3: detection limit for at least three grains; $_{pL}$: probability level assigned to the detection limits; MSWD: mean square of weighted deviates. The MSWD and the probability given for the concordia ages are for both concordance and equivalence (Ludwig, 2012, 1998). na: non applicable.

Bold: youngest maximum depositional age of the sedimentary unit, *Italic*: maximum depositional ages not fulfilling the 3 grains criterion.